The Spatial Atlas of Human Anatomy (SAHA): A Multimodal Subcellular-Resolution Reference Across Human Organs

Jiwoon Park[1,2], Roberto De Gregorio[1,3], Erika Hissong[1,4], Elif Ozcelik[1], Nicholas Bartelo[1], Felipe Segato Dezem[5,13], Luke Zhang[5,6], Maycon Marção[5,6], Hannah Chasteen[5,6], Yimin Zheng[7], Ernesto Abila[7,8], Junbum Kim[1], Jacqueline Proszynski[1], Akua A. Agyemang[1], Mohith Reddy Arikatla[1], Evelyn Metzger[9], Stefan Rogers[9], Prajan Divakar[9], Parambir S. Dulai[10,11], Jason Reeves[9], Yan Liang[9], Liuliu Pan[9], Sayani Bhattacharjee[9], Kimberly Young[9], Ashley Heck[9], Mithra Korukonda[9], Dan McGuire[9], Lidan Wu[9], Aster Wardhani[9], Joseph Beechem[9], George Church[2], Steven M Lipkin[1], Sanjay Patel[1,4], Fabio Socciarelli[1,4], Sebastien Monette[12], Brian Robinson[1,4], Massimo Loda[1,4], Olivier Elemento[1,3], Luciano Martelotto[13,*], Jasmine Plummer[5,6,14,15,*], André F. Rendeiro[7,8,*], Alicia Alonso[1,3,*], Robert E. Schwartz[1,*], Shauna Lee Houlihan[1,3,*], Christopher E. Mason[1,]

Affiliations:
[1] Weill Cornell Medicine, New York, NY, USA
[2] Harvard Medical School, Boston, MA, USA
[3] Caryl and Israel Englander Institute for Precision Medicine, Weill Medical College of Cornell University, New York, USA
[4] Department of Pathology and Laboratory Medicine, Weill Medical College of Cornell University, New York, NY, USA
[5] Center for Spatial Omics, St. Jude Children's Research Hospital, Memphis, TN, USA
[6] Department of Developmental Neurobiology, St. Jude Children's Research Hospital, Memphis, TN, USA
[7] CeMM Research Center for Molecular Medicine of the Austrian Academy of Sciences, Vienna, Austria
[8] Ludwig Boltzmann Institute for Network Medicine at the University of Vienna, Austria
[9] Bruker Spatial Biology, Seattle, WA, USA
[10] Department of Medicine, Division of Gastroenterology and Hepatology, Northwestern University Feinberg School of Medicine
[11] Center for Human Immunobiology, Northwestern University Feinberg School of Medicine
[12] Memorial Sloan Kettering Cancer Center, New York, NY, USA
[13] University of Adelaide, Adelaide, Australia
[14] Comprehensive Cancer Center, St. Jude Children's Research Hospital, Memphis, TN, USA
[15] Department of Cellular & Molecular Biology, St. Jude Children's Research Hospital, Memphis, TN, USA

*Corresponding author(s); Main contact: Christopher E. Mason (chm2042@med.cornell.edu)

ABSTRACT

The Spatial Atlas of Human Anatomy (SAHA) represents the first multimodal, subcellular-resolution reference of healthy adult human tissues across multiple organ systems. Integrating spatial transcriptomics, proteomics, and histological features across over 15 million cells from more than 100 donors, SAHA maps conserved and organ-specific cellular niches in gastrointestinal and immune tissues. High-resolution profiling using CosMx SMI, 10x Xenium, RNAscope, GeoMx DSP, and single-nucleus RNA-seq reveals spatially organized cell states, rare adaptive immune populations, and tissue-specific cell-cell interactions. Comparative analyses with colorectal cancer and inflammatory bowel disease demonstrate the power of SAHA to detect disease-associated spatial disruptions, including crypt dedifferentiation, perineural invasion, and therapy-resistant immune remodeling. All data are openly accessible through a FAIR-compliant interactive portal to support exploration, benchmarking, and machine learning model training. Through SAHA, we provide a foundational framework for spatial diagnostics and next-generation precision medicine grounded in a comprehensive human tissue atlas.

INTRODUCTION

Human tissues normally maintain structural integrity and function across diverse physiological states, but how these architectures break down in disease, aging, and stress remains a fundamental yet largely unresolved question in biology and medicine. The advent of spatial omics technologies has transformed our ability to map gene and protein expression within intact tissues, offering subcellular-resolution insights into cellular interactions and tissue architecture [1], [2]. Yet a critical gap remains: there is no comprehensive spatial reference of healthy human tissues across multiple organ systems. Existing atlases, including the Human Cell Atlas [3], Human Protein Atlas, and Human Tumor Atlas Network [4], have advanced our understanding of single-cell biology, but are largely derived from dissociated cells or disease-specific samples, limiting their utility as healthy spatial baselines [5].

To address this critical need [6], we established the Spatial Atlas of Human Anatomy (SAHA)—the first multimodal, subcellular-resolution reference atlas of healthy adult human tissues spanning gastrointestinal and immune systems. SAHA integrates spatial transcriptomic, proteomic, and histological data from over 100 diverse donors, capturing cellular organization at ~50 nm resolution. Unlike prior efforts, SAHA implements a rigorously standardized pipeline for tissue procurement, processing, quality control, and cross-platform integration. Our initiative enables consistent, reproducible analysis across organs, individuals, and spatial profiling technologies, while preserving the architectural context often lost in dissociated single-cell studies.

SAHA not only provides a high-resolution baseline of normal tissue organization but also facilitates comparative analyses with diseased tissues, enabling identification of spatially defined pathologies such as immune-epithelial remodeling, crypt dedifferentiation, and rare invasive niches. Through an open-access, FAIR-compliant [7] data portal (link to be updated

upon acceptance), SAHA aims to serve as a foundational benchmark for translational research, computational modeling, and spatially informed diagnostics [8].

Here, we report the first phase of SAHA encompassing 16 gastrointestinal and immune tissue types and demonstrate its utility for spatially resolved analysis of diseases, such as colorectal cancer, pancreatic cancer, and inflammatory bowel disease. SAHA represents the largest subcellular resolution, multimodal transcriptomic and proteomic dataset of healthy human tissues to date, enabling the characterization of both conserved and organ-specific spatial niches. Through comparative analyses with diseased cohorts, we illustrate SAHA's translational potential as a reference framework for identifying pathological alterations. By bridging spatial molecular profiling with clinical precision medicine, SAHA establishes a new paradigm for functional tissue atlasing and a blueprint for the next generation of spatial omics research.

RESULTS

1. Overview of the first gastrointestinal and immune spatial organ atlas

The first phase of the Spatial Atlas of Human Anatomy (SAHA) systematically mapped major digestive and immune organs at subcellular resolution, capturing over 15 million cells from over 100 healthy adult donors (ages 27-81 years, **Supplementary Table 1**). Using multiple high-plex spatial platforms including CosMx™ Spatial Molecular Imager, Xenium, RNAscope, and GeoMx® Digital Spatial Profiler, we captured high-resolution profiles of stomach, liver, pancreas, small intestine (ileum), large intestine (descending colon and appendix), bone marrow, and lymph nodes. To provide a molecular bridge between spatially resolved tissue architecture and a readily available systemic readout, we also included peripheral blood mononuclear cells (PBMCs), which represent a non-solid tissue component (**Fig. 1, Supplementary Table 2**). Across these efforts, we profiled 15,915,616 cells, including 9.5 million tissue-resident cells and 6 million circulating blood cells, at a spatial resolution of 50 nanometers. For the normal reference tissues, the CosMx RNA (1000-plex) dataset included 94 tissue samples, profiling 2.9 million cells and capturing over 524 million individual transcript measurements. This 1000-gene spatial atlas represents a substantial advancement in transcriptomic resolution—enabling detailed cell type phenotyping and cell–cell interaction analysis while preserving subcellular spatial fidelity. The corresponding CosMx protein dataset (67-plex) profiled 3.5 million cells and yielded over 17.8 billion quantified protein features. In contrast, disease and PBMC samples were analyzed using expanded RNA panels (6000-plex or 19,000-plex), providing deeper molecular coverage for characterizing rare populations and disease-specific states.

Standardized tissue collection and rigorous quality control were implemented to minimize batch effects and cross-platform variability, ensuring robust data integration and downstream analysis [9] (See **Methods**, **Extended Data Fig. 1, Supplementary Table 2**). This enabled joint analysis of transcriptomic profiles across organs, revealing both conserved and organ-specific cellular identities. Uniform Manifold Approximation and Projection (UMAP) of combined CosMx RNA data demonstrated distinct clustering of major epithelial lineages—such as hepatocytes (liver), acinar and ductal cells (pancreas), and gastric parietal and chief cells (stomach)—alongside

127 broad immune populations including T cells, B cells, macrophages, and dendritic cells (**Fig. 2a,**
128 **Extended Data Fig. 2a**). In total, over 50 distinct cell types were annotated using canonical
129 marker genes, encompassing broad epithelial, immune, stromal, and neuronal lineages,
130 highlighting both conserved and organ-specialized programs of cellular diversity and relative
131 abundance (**Fig. 2b-d**).
132
133 Subcellular resolution enabled precise localization of transcripts and proteins within individual
134 cellular compartments, allowing us to map the anatomical distribution of billions of biomolecules
135 across tissue sections. While higher resolution can increase technical variability and noise, our
136 quality control strategy (i.e., histopathological review, quantification of control probes,
137 RNAscope-based RNA integrity assessment, and platform cross-validation) ensured robust
138 reproducibility across tissues and donors (**Extended Data Fig. 3**). For example, RNAscope
139 control probes (i.e., *PPIB*) benchmarked RNA quality, and Spearman correlation analyses
140 demonstrated a strong monotonic relationship ($\rho = 0.86$, $p = 0.0007$) between RNAscope and
141 CosMx transcript measurements, without significant systematic bias, while CosMx maintained
142 greater transcriptome coverage due to its higher plex capacity (**Extended Data Fig. 3a-c**).
143 Together, these analyses establish the technical reproducibility and biological validity of SAHA
144 datasets and cell annotations, enabling robust cross-organ and cross-platform comparisons and
145 providing a reliable reference for future spatial studies. Quality metrics across sample cohorts
146 were highly consistent (**Extended Data Fig. 3d**), underscoring the robustness of the integrated
147 data resource. This inaugural phase of SAHA establishes the largest high-quality, multimodal
148 spatial reference of the human digestive and immune systems at subcellular resolution—
149 providing a foundational resource for investigating tissue architecture, cellular diversity, and
150 microenvironmental organization in health and disease.
151
152
153 **2. Cellular neighborhoods and interactions across intestinal and immune structures**
154 Leveraging an integrated embedding of over 15 million spatially profiled cells, SAHA enables
155 both cross-organ comparisons and high-resolution analysis of spatial architecture within and
156 across organ systems, tissue types, and cell populations (**Fig. 2**). This flexible framework
157 supports multiscale investigation of tissue organization and microenvironmental interactions. In
158 the gastrointestinal system, high-plex spatial profiling revealed nuanced, layer-specific
159 architectures and discrete cellular niches spanning the epithelium and underlying submucosa
160 (**Fig. 3a**). In the colon, for instance, epithelial crypts were distinctly segmented, with *PIGR* and
161 *MHC-I* expression localized to mucosal and submucosal regions, and smooth muscle markers
162 (e.g., *ACTA2*) confined to the muscularis layer. Cell-level adjacency mapping further uncovered
163 localized immune infiltration at crypt boundaries, suggesting active epithelial-immune crosstalk
164 that is not readily detectable in dissociated single-cell datasets.
165
166 SAHA provides a topographical link between structure and single-cell activity. Analysis of
167 regionally enriched gene programs demonstrated spatial specialization along tissue depth axis
168 (**Fig. 3b**). Surface regions were enriched for keratinization-associated signatures, whereas
169 deeper crypt zones expressed genes involved in antigen-processing and presentation. Spatial
170 mapping of cell cycle regulators (e.g., *CDKN1A*, *CCND1*) and stress-response genes (e.g.,

171 *TFEB*) showed selective enrichment at immune-rich epithelial interfaces, suggesting localized
172 zones of proliferative and immunomodulatory adaptation (**Fig. 3c**). Unbiased clustering of cell-
173 cell adjacency networks further delineated distinct cellular neighborhoods across crypt and
174 submucosal compartments (**Fig. 3d-f**). Discrete microenvironments dominated by epithelial cell
175 to T cells, B cells, or myofibroblast interactions emerged along the crypt-luminal axis,
176 emphasizing substantial spatial heterogeneity even within morphologically similar layers. These
177 findings highlight the unique power of subcellular-resolution spatial profiling to uncover
178 microanatomical, structural features that are inaccessible through dissociated single-cell
179 approaches.
180
181 Beyond crypt-associated immune niches, gastrointestinal organs also revealed highly organized
182 lymphoid structures. In the appendix (**Fig. 3g, Extended Data Fig. 4**), we identified large
183 lymphoid aggregates composed of interspersed T and B cells, surrounded by mesenchymal and
184 myeloid populations. Force-directed graph visualizations of cell-cell adjacency networks
185 demonstrated dense immune-immune interactions within these aggregates, consistent with their
186 role as specialized hubs for adaptive immune activation (**Fig. 3h**). UMAP embeddings
187 annotated by both broad and fine-grained cell identities highlighted tight spatial co-localization of
188 functionally distinct immune subsets, including T follicular helper cells and germinal follicle
189 center B cells (**Fig. 3i**). Ligand-receptor interaction analyses further revealed frequent paracrine
190 signaling among these populations, suggesting coordinated immunological activity within these
191 spatially confined niches (**Fig. 3j**).
192
193 These lymphoid aggregates occupy anatomically defined regions within gastrointestinal tissues
194 and serve as sites of antigen presentation, lymphocyte activation, and localized immune
195 coordination. To assess the generalizability of such spatially organized immune niches, we
196 compared them with canonical germinal centers (GCs) in lymph nodes (LNs). Unsupervised
197 clustering and spatial mapping of LN datasets revealed distinct compartmentalization between
198 GC-resident B cells and surrounding immune and stromal populations (**Fig. 4a, Extended Data**
199 **Fig. 5a-b**). Differential expression analysis further highlighted this organization, with B cell and
200 antigen presentation genes (e.g., *CD74*, *CD79A, HLA-DRA*) enriched in GC cores (q-values =
201 5.47×10^{-34}, 1.89×10^{-10}, 1.20×10^{-20}), while stromal and chemotactic transcripts (*CCL21, CXCL12,*
202 *VIM*) localized to adjacent zones (q-values = 3.18×10^{-99}, 7.21×10^{-24}, 4.84×10^{-20}) (**Extended Data**
203 **Fig. 5c-f**).
204
205 To compare gut-associated lymphoid structures with canonical germinal centers, we analyzed
206 anatomically paired epithelial (APE) lymphoid aggregates in the gastrointestinal tract. Similar to
207 lymph node GCs, intra-GC B cells in APE structures expressed *IGHG1* and *IGKC*, while
208 surrounding stromal regions were enriched for *APOE* and extracellular matrix genes (**Fig. 4c,**
209 **Extended Data Fig. 5g**). However, unlike the sharply zonated architecture of lymph nodes,
210 APE lymphoid structures were embedded within a more intermixed environment of epithelial
211 and mesenchymal cells (**Fig. 4d-e**), suggesting greater potential for immune-epithelial crosstalk.
212 conserved and tissue-specific transcriptomic gradients across GC and peri-GC regions in LN
213 versus APE, highlighting organ-specific spatial organization (**Extended Data Fig. 5h**).
214

Expanding our analysis across all SAHA gastrointestinal tissues—including appendix (APE), ileum (ILE), colon (COL), and stomach (STO)—we profiled 43 patient samples comprising 948 fields of view (FOVs) and over 1.15 million spatially resolved cells (**Fig. 4g**). Integrative clustering of transcriptomic profiles combined with spatial adjacency information identified three major niche types: (1) organ-shared epithelial-immune interaction zones, (2) organ-specific immune microenvironments within lymphoid structures, and (3) rare cell populations with distinct spatial distributions (**Fig. 4h-k, Extended Data Fig. 6**). Shared epithelial-immune neighborhoods, characterized by dense T- and B-cell infiltration adjacent to crypt structures, were recurrently observed in both colon and ileum samples (**Fig. 4h-i, Extended Data Fig. 6a-d**). In contrast, the stomach exhibited parietal-chief cell clusters unique to gastric glands, and the appendix contained specialized adaptive immune hubs, reflecting tissue-specific adaptations of immune-epithelial architecture (**Fig. 4j-k**).

To investigate the functional roles of these spatial niches, we leveraged the unique ability of spatial data to profile the ligand-receptor interaction networks between shared and organ-specific microenvironments. Conserved immune-epithelial niches were dominated by paracrine signaling between compartments, whereas tissue-specific structures exhibited distinct adaptive immune signaling profiles (**Extended Data Fig. 6e**). Complementary spatial variance analysis revealed that genes involved in immune activation (e.g., *CD74*, *IGHM*), epithelial barrier integrity (e.g., *PIGR*), and chemokine signaling (e.g., *CCL21*) were highly localized within discrete spatial clusters (**Fig. 4l**). These findings suggest that spatial neighborhoods are defined not only by their cellular composition but also by localized transcriptional programs. Collectively, these analyses demonstrate that spatial information is essential for uncovering hierarchical tissue organization, functionally specialized microenvironments, and organ-specific immune architecture in the human gastrointestinal tract.

3. Validation and integration of multimodal spatial data

The detailed spatial mapping of gastrointestinal tissues highlights the power of subcellular-resolution atlases to uncover structured microenvironments and immune-epithelial interactions. To ensure the robustness and biological fidelity of these insights across platforms and tissues, we systematically validated SAHA datasets through multimodal integration of spatial transcriptomic and proteomic data; we performed cross-platform validation using orthogonal spatial assays, including CosMx RNA and protein profiling, 10x Genomics Xenium, RNAscope, GeoMx DSP, and histopathology-based annotations (**Supplementary Table 2**).

In particular, integration of CosMx RNA and protein data enabled single-cell-level validation of biological consistency and facilitated deeper characterization of cell states and subtypes. Co-embedding of 1000-plex CosMx RNA and 67-plex CosMx protein profiles preserved tissue structure and cellular identities, confirming the robustness of multimodal spatial profiling (**Fig. 5a, Extended Data Fig. 7a-b**). Canonical markers such as CD45 (PTPRC), E-cadherin (CDH1), CD3D, and CD20 (MS4A1) exhibited concordant expression across RNA and protein modalities (**Fig. 5b-d**). Protein-based annotations aligned closely (Adjusted Rand Index, ARI = 0.2719)

with RNA-integrated labels using Maxfuse [10], supporting consistent cell type classification across modalities and batches (**Fig. 5c, Extended Data Fig. 7c-d**). Protein data also provided clearer delineation of architectural features, such as the epithelial-stromal interface in the stomach and lymphoid aggregates in the appendix (**Fig. 5d**), reflecting the stability, localization, and abundance of structural proteins relative to transcriptomic signals [11]. Transcriptomic profiles offered broader molecular coverage, enabling finer discrimination of epithelial subtypes and detection of rare populations such as stem and transit-amplifying cells.

Beyond validating cell identity and tissue structure, protein datasets offer orthogonal confirmation of receptor-ligand interactions inferred from RNA data (**Fig. 5e**) and provide direct evidence of translational activity. While such multimodal comparisons reinforce biological interpretation, it is important to note that RNA-protein correlations are not always linear. Although this discordance has been widely hypothesized, systematic large-scale comparisons across tissues have remained limited. Leveraging SAHA's multimodal resolution, we directly compared matched RNA and protein measurements across multiple organs (**Fig. 5f**). Housekeeping and structural genes such as VIM and FN1 showed strong concordance, whereas key immune and signaling molecules—including RELA and IGHD—displayed substantial discrepancies between RNA and protein levels (**Fig. 5f, Extended Data Fig. 7e-f**). These differences were further highlighted in cross-organ analyses: VIM exhibited consistent RNA-protein correlation across tissues (R^2 = 0.5781 with p-value = 0.0026 when compared across all SAHA cells), whereas IL1B showed widespread RNA expression with minimal protein detection. Conversely, CD276 demonstrated robust protein abundance despite low transcript levels, consistent with post-transcriptional regulation [12]. These comparisons underscore the necessity of multimodal profiling to accurately capture both transcriptional potential and protein-level function.

The integration of histopathology-based annotations with spatial molecular profiles reinforced biological interpretability and enabled precise mapping of anatomical features to molecular states. Histological landmarks such as crypt architectures, lymphoid aggregates, and smooth muscle layers corresponded closely to spatial clustering patterns observed in molecular datasets (**Fig. 6**). This alignment between morphology and molecular identity validates the technical robustness and biological fidelity of the SAHA datasets, supporting consistent cross-tissue, cross-platform, and cross-modality analyses at subcellular resolution.

To further harness histological information, we applied a multi-modal vision-text foundation model [13] that decodes tissue architecture from hematoxylin and eosin (H&E) stained whole-slide images (**Fig. 6a-b**). The model extracts quantitative morphological features from image tiles and learns spatial embeddings, which preserve anatomical continuity and discriminate between distinct structural zones (See **Methods**, **Fig. 6c-d**). Unsupervised clustering of these image-derived features reconstructed tissue organization, including epithelial boundaries, stromal interfaces, and muscular layers (**Fig. 6e**). Visualization of representative clusters using UMAP revealed discrete and biologically meaningful groupings that corresponded to histologically distinct morphotypes, such as crypt bases, glandular epithelium, and lymphoid-rich

regions most of which aligned with unbiased, RNA-based spatial clustering results (**Fig. 4g-k, 6f**).

This approach generalizes across gastrointestinal tissues, as image-derived embeddings from the colon, ileum, and appendix consistently show conserved morphological classes, including crypt epithelium, extracellular matrix, and immune niches (**Fig. 6g**). Morphological clusters overlapped with specific histopathological terms scored by the multi-modal vision-text model (**Fig. 6h**) and displayed enrichment for specific tissue compartments such as epithelial, connective, or immune components (**Fig. 6i**). Spatial adjacency patterns among clusters (**Fig. 6j**) and their correlations with RNA-derived cell type proportions (**Fig. 6k**) further confirmed that image-derived features captured biologically relevant gradients in tissue organization. Finally, direct comparison of H&E image and CosMx RNA projection revealed highly consistent alignment shown by positive CCA correlation, between image-based morphology and transcriptomically defined cell types (**Fig. 6l**), illustrating the power of histology-informed molecular modeling for spatial atlas construction.

4. SAHA's utility and impact in biomedical research

A key motivation for constructing SAHA was to enable comparative spatial analysis of diseased tissues, particularly in contexts where matched healthy controls are unavailable. To demonstrate its translational utility, we applied SAHA to two clinically relevant diseased conditions: colorectal cancer (CRC) and inflammatory bowel disease (IBD).

In CRC, we analyzed transcriptional and structural profiles in tumor adjacent crypt regions and compared healthy tissue (SAHA COL, $n = 3$) to histologically normal crypts from CRC resections ($n = 1$) (**Fig. 7a**). Crypt regions were stratified and annotated as 'top' and 'bottom' crypts, based on gene expressions and their locations (**Fig. 7b, Extended Data Fig. 8a-b**). Bottom crypts were identified by enrichment of genes associated with intestinal stem cells (*OLFM4*) and differentiated secretory cells (*LEFTY1, STMN1*), whereas top regions expressed mature epithelial markers (e.g., *KRT20, PLAC8, CEACAM1*). Notably, crypts adjacent to CRC exhibited disruption in spatial expression patterns; markers normally restricted to bottom regions (i.e., *H2AZ1, SPINK1*) were aberrantly expressed in the upper crypts, and vice versa for *CEACAM6* and *CEACAM1* (**Fig. 7c, Supplementary Table 3**). These patterns potentially indicate crypt dedifferentiation and spatial disorganization often associated with tumor formation [14], [15].

Tumor-adjacent crypts also harbored a distinct transcriptional program with genes significantly more differentially expressed than in healthy crypts (**Fig. 7c**). Several upregulated genes, including *REG1A*, have been previously associated with poor prognosis and crypt-inflammation in CRC, while upregulation of *IL6* and *IL22* receptors are known to promote inflammation and tumor development in CRC [16], [17]. CRC-associated crypts had a substantially higher number of differentially expressed genes (DEGs) compared to COL crypts, indicating broader transcriptional reprogramming (i.e., 96 vs 61 DEGs in bottom crypt and 116 vs. 72 DEGs in top crypt; **Supplementary Table 3**). In terms of the tumor microenvironment, FOVs profiled from

345 CRC samples showed a significant increase in the number of mast cells (**Extended Fig. 9c**), a
346 known driver of angiogenesis and metastasis [18].
347
348 To further investigate spatial expression and organization of RNA transcripts, we performed
349 spatial autocorrelation analysis using Moran's I and clustered FOVs based on their top 200
350 spatially variable genes (SVGs) (**Fig. 7d**). This unsupervised approach effectively distinguished
351 crypts from CRC and COL samples, indicating their divergent spatial states. From matched top
352 and bottom crypt compartments across conditions, we visualized all SVGs and identified both
353 conserved spatial markers (e.g., *KRT20, CEACAM1, CEACAM6*) and spatially enriched
354 disease-associated genes (e.g., *REG1A, IL22RA1*) - both of which were also noted in our
355 differential expression analysis (**Fig. 7e-f, Extended Data Fig. 8e**).
356
357 Beyond structural comparisons, SAHA enabled exploration of intrapatient tumor heterogeneity
358 (**Fig. 7g-j**), including rare events such as perineural invasion (PNI) (**Fig. 7k-m**). Within a single
359 CRC sample, we identified two spatially and transcriptionally distinct tumor subtypes (labelled
360 as Type 1 and Type 2), based on dominant cell compositions and immunogenicity (**Fig. 7g**).
361 Type 1 tumor regions exhibited a higher lymphocyte to tumor ratio with increased proportions of
362 cytotoxic and naive CD8+ T cells, whereas Type 2 regions were enriched for macrophage
363 subsets (**Fig. 7g-j, Extended Data Fig. 8f-g**).
364
365 Among the analyzed FOVs, we captured a rare perineural invasion event, characterized by
366 dysplastic stroma surrounding a nerve and tumor cells encircling the perineurium (**Fig. 7k**).
367 Although perineural invasion is recognized as a hallmark of aggressive CRC, it remains difficult
368 to resolve with conventional histopathology and immunofluorescence, which lack
369 comprehensive transcriptomic resolution. While recent single-cell RNA-seq studies have
370 attempted to profile these events, they often fail to capture neural cells altogether—or, if
371 captured, cannot confidently localize them or distinguish whether they are part of a PNI
372 structure or simply present in unrelated regions of the tissue [19]–[21]. By leveraging the spatial
373 context of SAHA, we subclustered this PNI region and uncovered a rare subset of fibroblasts
374 (less than 100 cells in the PNI region) in close proximity to glial cells, characterized by a hybrid
375 transcriptional signature expressing both glial-associated genes (*CLU, NGFR, SLC2A1, APOD*)
376 and cancer-associated fibroblast markers (<2% of fibroblasts identified in the sample) such as
377 *CXCL14* and *MMP2* (**Fig. 7k-l, Extended Data Fig. 8h**). Cell-cell communication analysis
378 further revealed unique signaling pathways within the PNI niche, including the ANGPTL
379 pathway originating from fibroblasts, previously associated with increased metastatic risk in
380 CRC [22]–[24], and the LIFR pathway, exclusively signaling from tumor cells to glial cells,
381 known to facilitate tumor-fibroblast crosstalk and activate pro-invasive programs [25]. These
382 findings offer new insights into the interactive dynamics within this rare microenvironment and
383 its ability to specify high resolution details of rare tumor types.
384
385 We also compared SAHA ILE with ileal samples from patients with inflammatory bowel disease
386 (IBD), including individuals stratified by clinical response to TNFα inhibitor therapy (**Fig. 8a**).
387 Integration of CosMx RNA profiles across healthy and IBD ileum samples revealed clear
388 separation by disease state, while preserving major cell type identities (**Fig. 8b, Extended Data**

389 **Fig. 9a-b**). Correlation analysis of average gene expression profiles demonstrated strong
390 consistency (e.g., spearman correlation of 0.74 for epithelial cells from 1K and 6K datasets)
391 across datasets generated with different plex sizes, validating the reproducibility of cell-type
392 transcriptional programs (**Extended Data Fig. 9a**). Spatial mapping of cell types demonstrated
393 increased immune cell infiltration into epithelial compartments in IBD samples relative to healthy
394 controls (**Fig. 8c, Extended Data Fig. 9c-d**).
395
396 Quantification of epithelial-proximal immune infiltration within 300 μm confirmed a significant
397 increase in immune cell density in IBD tissues ($p < 0.001$; **Fig. 8d**). Ligand–receptor interaction
398 analyses further revealed enhanced immune-epithelial signaling in IBD, particularly among non-
399 responders to TNFα therapy, who exhibited elevated spatial interaction scores relative to
400 responders (**Fig. 8e**). Mesenchymal-stromal populations in IBD tissues showed increased
401 expression of pro-inflammatory and extracellular matrix remodeling markers, including elevated
402 *TNFRSF1A* (TNF receptor 1) expression among non-responders compared to responders ($p <$
403 0.05; **Fig. 8f**). Spatial mapping of TNF-TNFRSF1A ligand–receptor interactions localized active
404 signaling to immune-mesenchymal interfaces, particularly in non-responder tissues (**Fig. 8g**).
405
406 These molecular level changes were consistent with the histological analyses. As performed for
407 the healthy GI tract (**Fig. 6**), we applied a multi-modal text-vision model to quantify and describe
408 the morphological patterns of H&E-stained ileum sections of healthy and IBD tissues (**Fig. 8h**).
409 IBD samples were distinguishable from healthy, with histopathological terms related to
410 metaplasia, immune cell infiltration, crypt branching, and apoptosis more frequent in IBD
411 samples compared to controls (**Fig. 8i**). Furthermore, we also found differentially enriched
412 morphological changes in response to TNFα treatment (**Fig. 8i**), which were aligned with
413 molecular findings, reinforcing the multi-layered disruption of epithelial and stromal architecture
414 in IBD [26]. These analyses demonstrate how SAHA enables spatially resolved comparisons of
415 healthy and diseased tissues at both molecular and histological levels, providing critical insights
416 into disease-associated microenvironmental changes and therapeutic response heterogeneity.
417
418 The integration of spatial transcriptomics and proteomics extends the analytical frameworks
419 traditionally applied to single-cell sequencing by adding critical layers of structural and
420 contextual information (**Fig. 9a**). Spatial multi-omics enables not only transcriptomic and
421 proteomic profiling at subcellular resolution, but also the characterization of extracellular matrix
422 (ECM) features, direct cell-cell interactions, and subcellular biomolecule localization, which are
423 dimensions inaccessible to dissociated single-cell methods. The addition of spatial context
424 enables direct measurement of cellular phenotypes, resolving the challenge of drawing
425 conclusions from disconnected data. This multidimensional mapping redefines efforts in building
426 biological atlases and opens new avenues for understanding tissue organization and function.
427
428 Recent technological advances now enable high-throughput, same-cell spatial multi-omics at
429 subcellular resolution—capturing whole-transcriptome RNA (~19,000 genes), high-plex protein
430 expression (~67 markers), and histological context within a single assay (**Fig. 9a**). These spatial
431 platforms also provide cell morphology, boundary, and segmentation data that are inaccessible
432 via traditional dissociated single-cell methods. To scale this approach across large tissue

volumes and billions of cells, we implemented computational workflows capable of integrating transcriptomic, proteomic, and morphological data at population scale. Compared to conventional scRNA-seq, spatial multi-omics approaches using Xenium and CosMx offer orders-of-magnitude lower cost per cell and support efficient scaling to billions of cells with fewer experimental runs—facilitating population-scale spatial atlasing (**Fig. 9b**).

To maximize accessibility and impact, SAHA adheres to the FAIR (Findable, Accessible, Interoperable, and Reusable) data principles. The SAHA data portal provides an open-access platform for exploring spatial multi-omics datasets, equipped with interactive visualization tools, high-resolution tissue navigation, and download capabilities for downstream analysis (**Fig. 9c**). Beyond serving as a reference, SAHA establishes standardized protocols and integration frameworks that can be adopted across institutions to enable scalable, reproducible spatial profiling.

DISCUSSION

The Spatial Atlas of Human Anatomy (SAHA) establishes the first multi-organ, multimodal, and multi-platform reference map of healthy human gastrointestinal and immune systems at subcellular resolution. By integrating histological, proteomic, and transcriptomic data across tissues and spatial technologies, SAHA addresses major limitations of previous atlasing efforts, which have predominantly relied on dissociated single-cell data and lacked spatial context. A key strength of SAHA lies in its rigorously standardized experimental and computational pipelines, which ensure reproducible, high-quality data generation and facilitate integrative analyses across organs and modalities. To support cross-platform consistency, we implemented systematic validation across CosMx, Xenium, GeoMx, and RNAscope platforms, alongside robust quality control metrics. While SAHA initially leveraged 1000-plex RNA profiling, we also introduce the field's first whole-transcriptome and paired protein multi-omics datasets at subcellular resolution—expanding beyond mid-plex spatial transcriptomics to unlock deeper biological insights and establish a future-ready reference for spatial biology.

A central innovation of SAHA lies in its multimodal design. The integration of RNA, protein, and histopathological (H&E) data facilitates both cross-validation of molecular signals and nuanced dissection of tissue structure and function. This multimodal synergy enabled identification of conserved spatial niches, lineage-specific expression gradients, and regionally restricted cell states, including rare and adaptive immune populations such as follicular B cells and intraepithelial lymphocytes. We also uncovered fine-grained epithelial and stromal subtypes, such as tuft and enterochromaffin-like cells, and delineated spatially encoded state transitions within common lineages—patterns that would be obscured in single-modality or dissociated datasets. Some segmentation ambiguity is inevitable in a subset of cells, in part due to the physical limitations of tissue sectioning through three-dimensional structures. However, we argue that such instances also encode meaningful biological information, as spatial proximity—retained in intact tissue—offers a critical dimension absent in single-cell suspensions. Dissociation-based workflows may also lose spatially tethered subpopulations during washing and library preparation steps. While future pixel-level or nucleus-aware segmentation methods

477 may refine these boundaries, our current analysis emphasizes broader tissue-level organization,
478 highlighting reproducible spatial relationships that extend beyond cell-intrinsic expression.
479
480 Across gastrointestinal tissues—including appendix, ileum, colon, and stomach—SAHA
481 captures a conserved layered organization spanning mucosa, submucosa, muscularis externa,
482 and serosa. At the same time, it reveals organ-specific features, such as crypt-villus gradients,
483 lymphoid aggregates (e.g., Peyer's patches), and vascular-rich stromal zones. These features
484 were consistent across individuals and histologically validated, reinforcing the atlas's technical
485 fidelity. Notably, cross-organ analysis within gastrointestinal tissues uncovered conserved
486 principles of mucosal organization while highlighting unique adaptations in the appendix, ileum,
487 colon, and stomach. A comparative profiling of lymphoid aggregates across GI organs and
488 matched germinal centers in lymph nodes revealed both preserved core immune architectures
489 and distinct spatial intermingling with epithelial and stromal compartments, emphasizing the
490 utility of SAHA in decoding tissue-specific immunological microenvironments.
491
492 Importantly, SAHA serves not only as a reference but also as an actionable spatial comparator
493 for disease studies—especially in clinical contexts where matched healthy tissue is unavailable.
494 We demonstrate this translational potential by benchmarking SAHA against datasets from
495 colorectal cancer (CRC) and inflammatory bowel disease (IBD). This revealed distinct
496 alterations in crypt top–bottom zonation, immune composition, and spatial gene expression
497 programs. For instance, spatial transcriptomics exposed crypt dedifferentiation in CRC and
498 aberrant cytokine signaling, while perineural invasion—an aggressive metastatic route—was
499 resolved at high granularity, highlighting glia-associated fibroblast states and tumor-nerve
500 signaling circuits. These examples illustrate how SAHA enables spatial biomarker discovery and
501 mechanistic insight into rare or complex pathological events, areas that have been briefly
502 explored in previous studies.
503
504 While SAHA represents a significant advance, several limitations remain. First, despite including
505 over 100 donors, our cohort size is modest relative to the full scope of human biological
506 diversity. Expanding SAHA across age groups, ancestries, and environmental exposures is
507 essential for broader generalizability. Second, although cross-platform integration across
508 CosMx, Xenium, GeoMx, and RNAscope demonstrates strong concordance, inherent technical
509 differences—such as probe capture efficiencies and antibody variability—necessitate ongoing
510 methodological harmonization. Third, this initial phase focuses on gastrointestinal and lymphoid
511 organs; a complete human reference will require comprehensive coverage across additional
512 anatomical systems.
513
514 While the current datasets represent the initial phases of spatial atlas construction, the platform
515 is designed for scalability and community-driven expansion. Active efforts are underway to
516 expand its organ coverage (second phase to genitourinary systems and additional immune
517 organs), apply whole-transcriptome and high-plex proteomics protocols, increase demographic
518 representation, and integrate advanced computational frameworks, including deep learning for
519 tissue segmentation and spatial graph modeling. We also aim to leverage Common Coordinate
520 Framework (CCF)-based registration and analysis pipelines to enable 3D spatial integration

521 across tissue sections and donors. This will support more anatomically precise mapping,
522 facilitate multi-plane reconstruction of tissue architectures, and allow in-depth cross-sample
523 comparisons at scale.
524
525 By integrating spatial molecular data with histological and clinical metadata, SAHA provides the
526 infrastructure for building digital twins of human tissues—enabling in silico simulations of
527 disease progression, therapeutic response, and tissue regeneration. These capabilities position
528 SAHA as a translational bridge between spatial biology and precision medicine, advancing both
529 fundamental research and clinical diagnostics. For example, we can extend SAHA toward
530 perturbation-aware modeling, using spatial benchmarks to assess disease-associated changes
531 and therapeutic responses—analogous to recent large-scale single-cell initiatives such as
532 Tahoe-100M [27]. Together, these directions will transform SAHA into a foundational tool for
533 spatially resolved systems biology and experimental medicine.
534
535 The SAHA data portal, built on FAIR (Findable, Accessible, Interoperable, Reusable) principles,
536 will enable broad community access and invite collaborative expansion. We envision that SAHA
537 will not only support basic biological discovery and accelerate clinical translation by providing a
538 standardized framework for the development of spatially informed diagnostics, prognostics, and
539 therapies. As spatial omics technologies continue to evolve, SAHA serves as a dynamic
540 foundation to integrate emerging data types, drive systems-level insights into tissue function and
541 disease, and chart new frontiers in precision medicine. We invite researchers worldwide to
542 utilize SAHA datasets, develop new analytical tools, and contribute additional spatial multi-
543 omics data to collectively accelerate biological discovery and the construction of a
544 comprehensive human spatial atlas.
545
546
547 **METHODS**
548 *Patient material, ethics approval, and consent for publication*
549 Human tissue samples were obtained from archived formalin-fixed, paraffin-embedded (FFPE)
550 blocks curated by board-certified pathologists and collaborating investigators (**Supplementary**
551 **Table 1**). Each tissue sample was selected from a diverse ancestry (if possible) from healthy
552 adults (no cancer or organ wide immune issues, ideal age 20-40). If tissues were difficult to get,
553 age and ancestry parameters can be compromised, but no cancer patients or patients with
554 diseases that will cause an impact on not diseased tissues was considered. Representative
555 fields of view (FOVs) were selected following comprehensive histopathological evaluation of
556 hematoxylin and eosin (H&E)-stained slides. Tissue acquisition and research use were
557 conducted under protocols approved by the Institutional Review Board (IRB) at Weill Cornell
558 Medicine, specifically IRB protocols 1306014012 (Hissong), 1008011210 (Robinson), and
559 107004999 (Inghirami). All experiments adhered to ethical guidelines, and consent for research
560 use of de-identified samples was obtained in accordance with IRB regulations.
561 Tissue microarray (TMA) formalin-fixed, paraffin-embedded (FFPE) blocks were constructed
562 following standard procedures. SAHA FFPE blocks were selected based on histopathological
563 evaluation, and representative areas were identified on hematoxylin and eosin (H&E)-stained
564 slides. Tissue cores (variable in diameter depending on the organ) were extracted using a

manual or semi-automated tissue arrayer and transferred into a pre-designed recipient paraffin block. The TMA block was re-embedded and cooled to ensure structural integrity. SAHA FFPE blocks were stored in cardboard boxes at room temperature (RT) under ambient humidity until the day of sectioning.

Tissue processing and histology

The FFPE blocks were sectioned at a thickness of 5 µm, and the sections were placed within Bruker's 15mm x 20mm allowed scan area on Leica Bond Plus slides (Leica Biosystems, S21.2113.A). Fresh ultrapure water was used to fill the water bath and new microtome blades were used for each tissue type. The first few sections from the block face were discarded. The number of serial sections to be collected was determined in advance according to the planned assays. Slides were labeled with a serial number to keep track of the order, ensuring that multiple assays were run on adjacent sections and facilitate subsequent data integration. If needed, one section, usually from the middle of the series, was dedicated to H&E staining, followed by full-slide image acquisition using the Aperio Digital Pathology Slide Scanner system (Leica Biosystems), allowing pathologists to identify and mark the area of interest in consideration of the available number of CosMx fields of view (FOVs). Most sections were also H&E stained after data acquisition. **Supplementary Table 2** lists the serial section numbers for each assay and for the corresponding H&E for each analyzed organ. Following sectioning, the slides were dried upright at RT for 30 minutes (min), followed by a horizontal overnight (ON) drying step at 37°C in an oven to improve tissue adherence. The slides were then stored in a desiccator at RT until processing. Most slides dedicated to the RNA assay were used within two weeks, as recommended by Bruker. Exact sectioning and run dates are reported in **Supplementary Table 2**.

CosMx processing

Processing of the slides followed the guidelines outlined in the Bruker manuals MAN-10184 for the RNA assay and MAN-10185 for the Protein assay, utilizing the equipment, materials, and reagents recommended in the manuals. Protocol details may have varied over time, reflecting updated manuals throughout the SAHA project. The specific manual version used for each assay is reported in **Supplementary Table 2**.

For the CosMx RNA assay, slides were baked at 60°C ON in vertical position in a baking oven. The following day, CitriSolv (VWR, 89426-268) was used for deparaffinization. Specifically, slides were brought to RT for 3 min, then subjected to two sequential 5 min immersions in CitriSolv, followed by two 5 min washes in 100% ethanol (Et-OH) (Sigma, E7023). The slides were dried vertically for 5 min at 60°C in the same baking oven. Antigen retrieval was conducted in a BioSB® TintoRetriever digital pressure cooker (BioSB, BSB 7015) at 100°C for 15 minutes. After the 5-minute drying step, slides were transferred into the preheated 1X Target Retrieval Solution (part of Bruker 121500006) as per the Bruker manual. The pressure cooker was then closed, and the temperature was allowed to return to 100°C. At this point, a 15 min timer was started, after which the slides were quickly rinsed up and down in DEPC water (Fisher Scientific, BP561-1) at RT for 15 seconds, washed for 3 min in 100% Et-OH, and then dried for 30 min horizontally on a clean surface at RT. 10 min before the end of the drying step, the incubation frame (part of Bruker 121500006) was applied to the slide and a 3 µg/mL Proteinase K (part of Bruker 121500006) working solution in 1XPBS (ThermoFisher Scientific, AM9625) was applied to the sections. The slides were then incubated for 30 min at 40°C in a RapidFISH slide hybridizer oven (Boekel

611 Scientific, 240200). During the final 10 min of digestion, Bruker fiducial beads (part of Bruker
612 121500006) were resuspended through alternating 1-min vortexing and 2-min sonication steps
613 (three vortexing steps and two sonication steps in total), then diluted in 2X SCC-T (part of Bruker
614 121500006). Fiducials were diluted at a final working concentration of 0.001% for Appendix,
615 Ileum, Colon, and Pancreas samples, 0.00075% for Stomach and Lymph Nodes samples, and
616 0.0005% for inflammatory bowel disease ileum samples. Following digestion, slides were washed
617 twice in DEPC water per the manual and then incubated with the prepared fiducials for 5 min,
618 protected from light at RT. The slides were then washed in 1XPBS for 1 min, fixed in 10% Neutral
619 Buffered Formalin (NBF) (EMS Diasum, 15740) for 1 min, washed twice in a 0.1M Tris-Glycine
620 NBF buffer solution for 5 min, once in 1XPBS for 5 min, and incubated with a freshly prepared
621 100 mM NHS-Acetate (Fisher Scientific, 26777) solution in NHS-Acetate buffer (part of Bruker
622 121500006) for 15 min in the dark at RT. Finally, the slides were washed twice in 2X SSC
623 (ThermoFisher Scientific, AM9763) for 5 min. At this point, slides were stored in 2X SSC,
624 protected from light, until it was possible to proceed with the ON hybridization step. The required
625 amount of probe for the run was transferred to 0.2 mL tubes, denatured for 2 min at 95°C in a
626 standard thermocycler, and crash-cooled on ice for 1 min. A probe hybridization mix containing
627 RNase inhibitors (Bruker, 121500004) and Buffer R (part of Bruker 121500006) was prepared
628 according to the Bruker manual. Slides were laid horizontally on a clean surface and the
629 hybridization mix was applied to the sections. A plastic coverslip (part of Bruker 121500006) was
630 then placed over the frame. The slides were incubated ON for 17-18 hours (h) at 37°C in the
631 RapidFISH slide hybridizer oven. The RNA probe panel used for the SAHA project was the
632 CosMx™ Human Universal Cell Characterization Panel (Bruker, 121500002), except for
633 inflammatory bowel disease ileum samples, which were run using the CosMx™ Human 6K
634 Discovery Panel (Bruker, 121500041). On the following day, after removing the coverslip, slides
635 were quickly rinsed in 2X SCC, washed twice for 25 min at 37°C in pre-warmed 50% 4X SSC/50%
636 formamide (ThermoFisher, AM9342), and washed again in 2X SCC twice for 2 min. The slides
637 were then incubated in the dark at RT for 15 min with a 1:40 dilution of DAPI (part of Bruker,
638 121500020) in blocking buffer (part of Bruker, 121500006). After a 5-min wash in 1XPBS, cell
639 segmentation marker staining was performed using a cocktail of CD298/B2M, PanCK, CD45, and
640 CD68 antibodies. The antibodies are conjugated to a readout domain that binds fluorophores on-
641 instrument. Slides were incubated in the dark at RT for 1 h with the morphology staining marker
642 mix, prepared using the CosMx™ Human Universal Cell Segmentation Kit, RNA (Bruker,
643 121500020) and the CosMx™ Human CD68 A La Carte Marker, RNA (Bruker, 121500022), at
644 the dilutions specified in the Bruker manual. Slides were then washed three times in 1X PBS for
645 5 min and transferred to 2X SSC. For most samples, the protocol spanned three days, meaning
646 that at this stage, the adhesive frame was removed, and slides were stored ON in 2X SSC at 4°C,
647 protected from light. The only exceptions were stomach and lymph node samples, which were
648 fully processed and loaded on the instrument in just two days. On the following day, the flow cells
649 were assembled using the Flow Cell Assembly Tool provided by Bruker and Bruker glass
650 coverslips with ports (CosMx™ Flow Cell Assembly Kit, Bruker, 122000061). They were then kept
651 in 2X SSC, ensuring the solution filled the flow cells to prevent section dehydration, and stored in
652 the dark until loading onto the CosMx instrument.
653 For the CosMx Protein assay, slides were baked for just 1 h at 65°C in a vertical position. Similar
654 to the RNA assay, after baking slides were equilibrated for 3 min at RT and then immersed in
655 CitriSolv twice for 5 minutes. In the case of the protein workflow, this was followed by a series of
656 washes: two 10 min washes in 100% Et-OH, two 5 min washes in 95% EtOH, one 5 min wash in
657 70% EtOH, and two 5 min washes in 1XPBS. The target retrieval step was performed as
658 described above for the RNA assay, with the only difference that after the 15 min retrieval, the

659 solution containing the slides was left to cool at RT for 25 min. The slides were then transferred
660 to 1XPBS and washed three times for 5 min. At this point, the incubation frame (part of Bruker
661 121500008) was applied to the slides. Sections were incubated with blocking Buffer W (part of
662 Bruker 121500008) for 1 h at RT, followed by ON incubation at 4°C with a single mix containing
663 both the morphology marker antibodies for segmentation (CosMx Human Universal Cell
664 Segmentation Kit, IO PanCK/CD45 Supplemental Segmentation Kit, and CD3 A La Carte Marker,
665 Bruker 121500026, 121500027, and 121500028) and the antibodies from the CosMx Human
666 Immuno-oncology 64-plex panel (Bruker, 121500010). The sections were covered with a plastic
667 coverslip (part of Bruker 121500008) during ON incubation. The following day, after removing the
668 coverslip, the slides were washed three times for 10 min in 1XTBS-T (ThermoFisher, J77500.K2)
669 and once for 2 min in 1XPBS. During the 1XTBS-T washes, fiducials were prepared as for the
670 RNA assay. For the protein assay, the final fiducial working concentration was 0.00005%,
671 requiring a two-step serial dilution in 1XTBS-T, as recommended by the manual. After a 5 min
672 incubation at RT with fiducials, slides were washed once with 1XPBS for 5 min, fixed with 4%
673 PFA (Electron Microscopy Sciences, 15710) for 15 min at RT in the dark, washed three times in
674 1XPBS for 5 min each, and incubated for 10 min at RT with a 1:40 dilution of DAPI (Bruker
675 121500026) in 1XPBS. The slides were then washed twice more in 1XPBS for 5 min, incubated
676 with freshly prepared 100 mM NHS-Acetate for 15 min protected from light at RT, and subjected
677 to a final 5 min wash in 1XPBS. As for the RNA assay, for most of the SAHA protein assays, the
678 protocol extended over three days. Slides were transferred to fresh 1XPBS tubes and stored at
679 4°C in the dark ON. On the following day, flow cells were assembled as described above, kept in
680 1XPBS in the dark, and loaded onto the CosMx instrument.
681 To set up a new CosMx runs on the Bruker CosMx Spatial Molecular Imager (SMI), the Bruker
682 manual MAN-10161 was used as a guide. Different versions of the manual were followed
683 throughout the SAHA project, and various SMI instrument software versions were installed on
684 the machine over time. **Supplementary Table 2** lists the instrument manual and software
685 versions for each analyzed sample. The SMI Control Center webpage interface allows for the
686 setup of all run specifications, as well as the assignment of FOVs. The setup begins with
687 configuring a new flow cell, the first step of which is defining the primary information for the run,
688 including the Pre-Bleaching Profile and the Cell Segmentation Profile. As these profiles are
689 tissue-type specific, they were selected based on Bruker's recommendations in MAN-10161, but
690 they ultimately ended up being Pre-Bleaching Profile C and Cell Segmentation Profile A for all
691 our runs, both RNA and protein. The probe panel and cell segmentation kits used also needed
692 to be specified at this stage. The sensor-based interactive SMI Control Center interface guided
693 the loading of the instrument. The Imaging Tray (CosMx RNA Imaging Tray, Bruker 122000156,
694 122000157, or 122000158, CosMx Protein Imaging Tray, Bruker 122000162 or 122000163),
695 flow cells, and buffers required for the run (CosMx RNA Instrument Buffer Kit, Bruker 100480 or
696 100481, CosMx Protein Instrument Buffer Kit, Bruker 100482) were loaded into their designated
697 slots. For RNA assays, RNase inhibitors (Bruker, 121500004) were added to a specific well of
698 the Imaging Tray. For all runs, two enzymes - Catalase and Pyranose Oxidase (part of Bruker
699 100480, 100481, and 100482) - needed to be resuspended, centrifuged, and added free of
700 precipitate to Buffer 4 in advance. Once the assembled flow cell were loaded onto the
701 instrument and all run parameters were approved, the system proceeded through a deck
702 validation step, an instrument preparation step, and a preliminary morphology marker scan to
703 allow the FOVs placement. RNA target readout on the CosMx SMI instrument was performed as
704 described in He et al. [28]. Reporter Wash, Imaging, and Strip Wash Buffers all supplied by
705 Bruker Spatial Biology. At this point, the FOV Selection Workspace opened, and the FOV
706 Placement Tool enabled for the placement, movement, or deletion of individual FOVs or grids of

707 FOVs over the scanned image of the section. For large tissue areas, a serial H&E scan was
708 used in advance by pathologists to annotate the image and define the regions of interest to be
709 covered by the available FOVs. For TMAs, we aimed to allocate a predefined number of FOVs
710 to individual tissue cores. Once the FOVs were reviewed and approved, the machine began
711 cycling. RNA readout began by flowing 100 µl of Reporter Pool 1 into the flow cell and
712 incubating for 15 min. Reporter Wash Buffer (1 mL) was flowed to wash unbound reporter
713 probes, and Imaging Buffer was added to the flow cell for imaging. Eight Z-stack images (0.8
714 µm step size) for each FOV were acquired, and photocleavable linkers on the fluorophores of
715 the reporter probes were released by UV illumination and washed with Strip Wash buffer. The
716 fluidic and imaging procedure was repeated for all the reporter pools, and the different rounds of
717 reporter hybridization (based on assay plex) imaging were repeated multiple times to increase
718 target detection sensitivity. Cell morphology was imaged on-instrument prior to RNA or protein
719 readout by adding fluorophore-bound reporters to the flow cell and capturing eight z-stack
720 images in the channels 488 nm (CD298/B2M), 532 nm (PanCK), 594 nm (CD45), 647 nm
721 (CD68), and 385 nm (DAPI). Runs lasted anywhere from two to ten days, depending on the
722 panel type and plex, and the number of FOVs. CosMx data were automatically uploaded to
723 Bruker's cloud-based AtoMx Spatial Analysis Platform both during and after the run.
724
725 *Single-nuclei sequencing (snPATHO-seq)*
726 Single nucleus RNA sequencing (snRNA-seq) was performed following the snPATHO-Seq
727 protocol as previously described [29]. Two scrolls of 30–50 µm thickness were obtained from
728 each FFPE sample, adjacent to the sections used for CosMx, Xenium, and H&E staining.
729 Scrolls were collected into 1.5-mL Eppendorf tubes, stored at 4°C in Ziplock bags containing
730 desiccants to control humidity, and processed within one week. For nuclei isolation, scrolls were
731 dewaxed by three sequential washes in 1 mL of xylene (Millipore Sigma, 214736) for 10 minutes
732 each, with the first xylene wash performed at 55°C to enhance paraffin removal. Rehydration
733 was achieved through serial immersions in decreasing concentrations of ethanol (100% twice,
734 followed by 70%, 50%, and 30%; each for 1 minute) (Millipore Sigma, E7023), followed by a
735 single wash with 1 mL of RPMI 1640 medium (Gibco, 11875093).
736 Tissues were then digested in RPMI 1640 supplemented with 1 mg/mL Liberase TH (Millipore
737 Sigma, 5401151001) and 1 U/µL RNase inhibitor (Thermo Fisher Scientific, EO0382). The
738 scrolls were fragmented using a pellet pestle, and the digestion volume was adjusted to 1 mL.
739 Digestion proceeded at 800 rpm in a Thermomixer. Following digestion, 400 µL of EZ Lysis
740 Buffer (Sigma-Aldrich, NUC-101) was added, mixed, and centrifuged at 850 × g for 5 minutes at
741 4°C. The nuclei-containing pellet was resuspended in EZ Lysis Buffer with 2% BSA (Miltenyi,
742 130-091-376) and RNase inhibitor, then homogenized by pestle and pipetting. The suspension
743 was filtered through a 70-µm strainer (pluriSelect, 43-10070-50) and centrifuged. The nuclei
744 pellet was washed three times with 1× PBS containing 1% BSA (Gibco, 70011044), followed by
745 two washes with 0.5× PBS containing 0.02% BSA. Final resuspension was performed in 500–
746 1000 µL of 0.5× PBS with 0.02% BSA, depending on pellet size, and filtered through a 40-µm
747 strainer (pluriSelect, 43-10040-50).
748 Nuclei were quantified using the Luna-FX7 instrument with Acridine Orange/Propidium Iodide
749 staining (Logos). For immediate processing, nuclei suspensions were kept on wet ice. snRNA-
750 seq libraries were prepared using the Chromium X Controller (10x Genomics) and the
751 Chromium Fixed RNA Profiling Reagent Kits for multiplexed samples (Chromium Fixed RNA Kit,

752 PN-1000475; Chromium Next GEM Chip Q, PN-1000418; Dual Index Kit TS Set A, PN-
753 1000251), following the manufacturer's user guide (CG000527, Rev E). For cryopreservation,
754 nuclei suspensions were supplemented with 10% glycerol and 0.1× Enhancer (10x Genomics,
755 PN-2000482), rested on ice for 10 minutes, and stored at -80°C.
756 Hybridization was performed using 500,000–1.5 million nuclei per sample at 42°C for 20 hours.
757 Barcoding reagents BC1–BC4 were used. Post-hybridization washes were conducted in a
758 pooled setting according to the user guide with an additional wash step. Approximately 10,000
759 nuclei were targeted for capture per sample. An extra cycle was added during the pre-
760 amplification PCR step, and indexing PCR was optimized to achieve final library concentrations
761 between 50 and 200 nM. Library quality was assessed using a Fragment Analyzer 5200
762 (Agilent) and quantified using a Qubit Flex Fluorometer (Thermo Fisher Scientific). Libraries
763 were sequenced on an Illumina NovaSeq 6000 using a 28 × 10 × 10 × 90 bp read configuration,
764 targeting 20,000–30,000 read pairs per nucleus.
765 Transcript count matrices generated by Cell Ranger v8.0.0 (10x Genomics) were imported into
766 Seurat v5.0.1 for downstream analysis [30]–[34]. Doublet identification was performed using
767 scDblFinder v1.14.0 with a preset doublet rate of 10%, reflecting the expected frequency in
768 Single Cell Gene Expression Flex multiplexing experiments [35]. Quality control based on UMI
769 and gene count distributions identified a population of low-complexity droplets, which lacked
770 distinct transcriptomic signatures and were excluded from further analysis. Nuclei flagged as
771 doublets or containing fewer than 1,000 detected genes were removed, ensuring retention of
772 major cell populations as validated by comparison with the original dataset. Normalization and
773 highly variable feature selection were conducted using SCTransform with default parameters.
774 Dimensionality reduction was performed using principal component analysis (PCA), with the first
775 30 principal components guiding Uniform Manifold Approximation and Projection (UMAP)
776 embedding (RunUMAP) and Louvain clustering.
777
778 *Xenium Slide Preparation and In Situ Gene Expression Assay*
779 Sections for Xenium assays were prepared according to the *Xenium In Situ for FFPE—Tissue*
780 *Preparation Guide* (CG000578 Rev C, 10x Genomics) following the manufacturer's instructions.
781 Briefly, 5-µm-thick FFPE tissue sections were floated in an RNase-free water bath and mounted
782 onto the 10.45 mm × 22.45 mm sample area of Xenium slides (PN-3000941, 10x Genomics).
783 Slides were air-dried at room temperature for 30 minutes, followed by a 3-hour incubation at
784 42°C on a Xenium Thermocycler Adapter plate positioned atop a 96-well thermal cycler (C1000
785 Touch, Bio-Rad) with the lid open. Slides were further dried ON at room temperature in the
786 presence of desiccants.
787 Subsequent processing, including deparaffinization and decrosslinking, was performed following
788 the *Xenium In Situ for FFPE—Deparaffinization and Decrosslinking Protocol* (CG000580 Rev C,
789 10x Genomics). Slides were incubated at 60°C for 2 hours, equilibrated at room temperature,
790 then sequentially immersed in xylene (twice, 10 minutes each), 100% ethanol (twice, 3 minutes
791 each), 96% ethanol (twice, 3 minutes each), 70% ethanol (once, 3 minutes), and water (once,
792 20 seconds). Following rehydration, slides were assembled into Xenium cassettes and hydrated
793 with 1× PBS. Tissue sections were reverse crosslinked using a decrosslinking buffer containing
794 tissue enhancer, urea, and perm enzyme B at 80°C for 30 minutes, followed by multiple PBS-T
795 washes.

796 Slides were then processed according to the *Xenium In Situ Gene Expression User Guide*
797 (CG000582 Rev E, 10x Genomics). Gene expression profiling was performed using the Xenium
798 Human Multi-Tissue and Cancer Panel (10x-1000626), targeting 377 genes for prostate, ileum,
799 appendix, pancreas, and colon samples, and the Xenium Human Breast Panel (10x-1000463,)
800 targeting 380 genes for breast cancer samples. Probe hybridization involved probe denaturation
801 at 95°C for 2 minutes, crash-cooling on ice, equilibration to room temperature, and 17-hour
802 hybridization at 50°C. Post-hybridization, slides underwent standardized washes, ligation,
803 amplification, autofluorescence quenching, and nuclear staining following the manufacturer's
804 protocols.
805 Slides assembled into Xenium cassettes were processed using the Xenium Analyzer according
806 to the *Xenium Analyzer User Guide* (CG000584 Rev D/E, 10x Genomics). Instrument setup
807 included loading of the Xenium Decoding Consumables Kit (PN-1000487) with appropriate
808 wash buffers and reagents. Slides were scanned to image fluorescently labeled nuclei, and
809 fields of view (FOVs) were selected for sequencing. Data acquisition utilized the Xenium In Situ
810 software suite (v1.9 for standard samples; v2.0 for multimodal segmentation samples), with
811 simultaneous collection of gene expression and segmentation data for multimodal samples.
812 Post-run, slides were washed with PBS-T and stored at 4°C in the dark until further staining and
813 analysis.
814
815 *RNAscope for quality assessment*
816 Chromogenic in situ hybridization was performed on an automated stainer (Leica Bond RX,
817 Leica Biosystems, Deer Park, IL) with RNAscope 2.5 LS Assay Reagent Kit-Red (Cat. #
818 322150, Advanced Cell Diagnostics, Newark, CA) and Bond Polymer Refine Red Detection
819 (Cat. # DS9390, Leica Biosystems) following manufacturer's standard protocol. Positive control
820 probe detecting a housekeeping gene (human PPIB, cat # 313908, Advanced Cell Diagnostics)
821 and a negative control probe detecting bacterial (*Bacillus subtilis*) dapB gene (cat #312038,
822 Advanced Cell Diagnostics) were used to assess RNA preservation and detection, and absence
823 of non-specific signal, respectively. The chromogen was fast red and the counterstain
824 hematoxylin. Positive RNA hybridization was identified as discrete, punctate chromogenic red
825 dots under brightfield microscopy. Whole slide images were acquired with an Olympus VS200
826 slides scanner and VS200 ASW 4.1.1 software (Evident Scientific, Hamburg, Germany) using a
827 20X/0.80NA objective to generate whole slide images with a pixel size of 0.2738 µm. Image
828 analysis was performed with QuPath 0.5.1 software (Bankhead, P. et al. QuPath: Open source
829 software for digital pathology image analysis [36]. The positive cell detection and subcellular
830 detection algorithms were used to detect cells and hybridization dots (individual spots and
831 clusters), respectively. The mean number of estimated spots per cell was reported for each
832 sample. The analysis we performed and validated by a board-certified veterinary pathologist
833 (SM).
834
835 *Data processing and annotation*
836 For CosMx RNA and protein data, AtoMx Spatial Informatics Platform (SIP) was used for image
837 processing and preprocessing of raw data. A slight modification was applied to the foundational
838 pipeline available on the AtoMx platform (v1.3). For quality control, cells with the following
839 cutoffs were flagged as low-quality cells: total transcript counts less than 20, negative probe

840 counts more than 10%, count distribution 1, area outlier 0.01 (outlier p-value cutoff 0.01). FOV
841 QC was done with default settings (mean, FOV count cutoff 100). The negative control probe
842 quantile cutoff for target QC was set to 0.5, and detection was set to 0.01.
843 The datasets were normalized by scale factors and total counts, while 6k panels and combined
844 datasets were normalized using total count normalization for scaling. For organ-specific
845 analyses, count matrices were normalized using sc.pp.normalize_total() and log-transformed via
846 sc.pp.log1p() (Scanpy v1.9.3). Dimensionality reduction was performed using PCA, followed by
847 neighborhood graph construction (sc.pp.neighbors()) and UMAP embedding (sc.tl.umap()).
848 UMAP was generated with the following parameters: 50 PCs for clustering, 40 number of
849 neighbors, 0.01 minimum distance, 5 spread, Cosine distance metric, 0.25 data fraction. Spatial
850 networks were calculated based on the distance (50 um), and neighborhoods based on the
851 Jaccard cutoff of 0.099 and cosine distance. The datasets were exported for cell type annotation
852 and further downstream analysis. For initial automated cell type annotation of RNA data, we
853 used Insitutype [37] with organ-specific profile matrices derived from published single-cell and
854 spatial transcriptomics datasets (available via the SAHA GitHub repository; see **Code**
855 **Availability**). For protein data, cell phenotyping was performed using SCIMAP based on a
856 marker-guided gating strategy. Manual refinement was applied as needed following
857 unsupervised clustering to improve resolution of rare or ambiguous populations. Various
858 batches and organ types were integrated for analysis using Harmony [38].
859
860 *Organ-specific analyses*
861 To characterize lymphoid architecture in lymph nodes, we applied a multimodal spatial analysis
862 workflow. Spatial niche detection was performed using spaVAE [39], a dependency-aware
863 variational autoencoder model. Normalized lymph node datasets were input into spaVAE using
864 default parameters over 50 iterations. The resulting niche clusters were compared to Leiden-
865 based transcriptomic clusters for biological interpretability. Germinal centers (GCs) and peri-GC
866 regions were manually segmented using an interactive workflow implemented with
867 matplotlib.widgets.PolygonSelector and matplotlib.path.Path. Visualizations were generated in
868 Jupyter notebooks using %matplotlib tk, enabling real-time polygon annotation of GC
869 boundaries. Cells were classified based on spatial overlap as intra-GC, peri-GC, or non-GC.
870 For spatial cell–cell interaction analysis, neighborhood graphs were constructed using Squidpy's
871 sq.gr.spatial_neighbors() function. Cell–cell interaction matrices were generated with
872 sq.gr.interaction_matrix(), leveraging Leiden-inferred annotations to quantify contact frequencies
873 across annotated cell types within GCs and adjacent regions. Gene expression patterns were
874 visualized using Seaborn's clustermap() to highlight transcriptional diversity among niche
875 clusters. Spatial autocorrelation statistics were calculated using Moran's I
876 (sq.gr.spatial_autocorr()), excluding the top 1% of expression outliers. Genes with the highest
877 spatial variability were selected for downstream interpretation and figure display. To identify
878 differentially expressed genes (DEGs) between intra-GC and peri-GC compartments, we
879 applied Wilcoxon rank-sum tests (scipy.stats.ranksums()), followed by multiple hypothesis
880 correction using the Benjamini–Hochberg procedure (statsmodels.stats.multitest.multipletests()).
881 Genes with adjusted $p < 0.05$ and $|\log_2 FC| > 0.5$ were considered significant. Volcano plots
882 were generated to highlight key upregulated and downregulated genes across compartments.
883

884 *Comparison and integration of CosMx Protein and RNA data*
885 To annotate protein data, we used SCIMAP (v1.3.2), a gating-based hierarchical cell annotation
886 tool which takes a workflow with cell types noted by their marker genes to conduct cell typing
887 (**Extended Data Fig 7a**). Integration of CosMx RNA and protein data was performed using
888 MaxFuse (version 0.02). a Python (version 3.8.20) package that uses co-embedding, data
889 smoothing, and cell matching to integrate "weakly-linked" multi-modal omics data that have little
890 overlapping features [10]. Broad and granular annotations from RNA samples are integrated
891 into serial sectioned protein samples to generate protein cell type annotations. We generated
892 cell type mapping to analogous RNA and protein regions to create visual comparisons. To
893 conduct the concordance comparison between SCIMAP and Maxfuse annotations, we
894 examined how cells called by one modality are called by the other by calculating adjusted rand
895 index and mapping a matrix of cell counts for the cell types of both modalities as a heatmap.
896 For RNA-protein correlations and concordance comparisons, all analyses were conducted using
897 R version 4.4.3 and the following R packages: Seurat (v5.2.1), reticulate (v1.41.0), anndata
898 (v0.7.5.6), dplyr (v1.1.4), ggplot2 (v3.5.2), ggrepel (v0.9.6), reshape2 (v1.4.4), and
899 RColorBrewer (v1.1.3). No cell-wise or feature-wise filtering was applied to either the
900 transcriptomic or proteomic datasets for this analysis. We identified 53 features common to both
901 RNA and protein modalities across 15 matched tissue cross-sections from 9 different organs.
902 For each tissue pair, the mean RNA and protein expression levels for each common feature
903 were computed after excluding values equal to zero, to avoid bias from low-input
904 measurements. Mean values were also calculated at the organ level by averaging feature
905 expression across all tissue sections from the same organ. In addition, pooled averages were
906 computed by aggregating all features across all organs. To assess the relationship between
907 RNA and protein expression, we computed the log10-transformed mean expression values of
908 each feature and visualized them using scatter plots, with log10(RNA mean) on the y-axis and
909 log10(protein mean) on the x-axis. These plots were generated for tissue pairs, organs, and the
910 aggregated dataset. Linear regression models were fit to each of these comparisons using the
911 lm() function in base R, with the following formula: log10(RNA.mean) ~ log10(PRT.mean). We
912 also generated analogous plots and regressions to compare average RNA and protein
913 expression values across all common features within each tissue pair and organ. Spearman's
914 rank correlation coefficient was used to calculate RNA-protein correlations across organs and
915 genes.
916
917 *Comparative analysis of H&E images with spatial transcriptomics datasets*
918 Whole-slide H&E imaging data was processed using LazySlide [40]. Gastrointestinal tract
919 samples (appendix, colon, ileum) were segmented and tesselated with tiles of 512 pixels at 0.5
920 µm/pixel (~20X magnification). For each slide, we randomly sampled 250 tiles and extracted
921 high-dimensional morphological embeddings leveraging the CONCH multi-modal vision–
922 language model [13]. Subsampling was performed to ensure equal contribution of various
923 slides/tissue types. Tile embedding values were scaled, reduced with Principal Component
924 Analysis (PCA) and visualized using the Isomap (scikit-learn) or Uniform Manifold
925 Approximation and Projection (UMAP) algorithm [41] and clustered using the Leiden algorithm
926 [42] at resolution 0.5 with Scanpy [43]. For downstream interpretation, we assembled a panel of
927 79 histolopathological terms related to instestinal biology or pathology. We computed the

similarity between the text embedding of each term in each CONCH feature vector of each tile. Text embedding term values were compared between morphological clusters using a Wilcoxon test, and the top 3 most differential terms were used to describe each cluster.
In parallel, we applied CellViT [44] to the same whole-slide images to perform end-to-end nuclear segmentation and classification. Within each sampled tile, we quantified cell-type abundances (e.g., epithelial, immune, connective) and averaged these cellular proportions per morphological cluster previously derived by the CONCH features. To link tile-based morphological phenotypes with molecular cell-type composition, we performed canonical correlation analysis (CCA) implemented in scikit-learn between the relative abundance of each morphology cluster and the corresponding cell-type proportions inferred by the CosMx platform per tissue slide.

Integrative analysis of SAHA COL and CRC CosMx data

Downstream analysis was performed using Seurat (v5.0.1) [30]–[34] throughout to assess cell types and perform graph-based clustering. To harmonize gene probes across both datasets, gene probes targeting closely related genes (previously combined in an earlier spatial probe set but separated into individual genes in the current set) were merged. Specifically, genes originally represented as single combined probes (e.g., *CCL3/L1/L3, CXCL1/2/3*) were merged into single meta-probes by summing their expression values across individual gene measurements. A complete list of merged genes is available in **Supplementary Table 3**. Genes without common representation across both spatial datasets were excluded to ensure consistent comparisons. After matching the probes, each FOV in the CRC sample was matched to an FOV from the COL sample to achieve relatively equal cell numbers (Figure 7, Extended Data Fig. 8).
Following this process, raw count matrices from each object were exported and combined using the merge() function from Seurat. Normalization, scaling, and PCA calculation were performed using standard Seurat functions. Objects were then integrated using Seurat's IntegrateLayers() function with the Harmony algorithm [38] (parameters: theta = 2, lambda = 0.1). After integration, Uniform Manifold Approximation and Projection (UMAP) embedding was performed using 30 principal components (PCs). Clusters were defined using a resolution of 0.3, and low-quality cells (Cluster 11) were excluded based on low feature counts. Prior to marker identification, the JoinLayers() function was applied as recommended by Seurat developers. Cluster markers were identified using Seurat's FindAllMarkers() function (parameters: min.pct = 0.2, logfc.threshold = 0.5, adjusted p-value < 0.05; Supplementary Table X).
Differentially expressed unique genes highlighted in Fig. 7c were identified with the FindMarkers() function using the MAST test (min.pct = 0.1, logfc.threshold = 0.5, adjusted p-value < 0.05; Supplementary Table X). Spatially differentially expressed genes (Fig. 7d-f) were computed using the Voyager tool [45] to calculate Moran's I. Field of views (FOVs) were clustered based on the top 200 spatially variable genes per field using principal component analysis (25 PCs), followed by k-means clustering (k = 2) as visualized in Fig. 7d.
Visualizations were generated with Seurat's functions: UMAPs (Fig 7a, Extended Data Fig. f,h) (DimPlot), Dotplots (Fig. 7h-2, Extended Data Fig. b,g) (DotPlot), violin plots (Fig 7c and e , Extended Data Fig. a) (VlnPlot), and pseudo-spatial images (Fig 7g-4, h-2, Extended Data Fig. h-1) (ImageDimPlot). Bar plots (Fig 7g-3, Extended Data Fig. c,f) were created using dittoBarPlot from dittoSeq [46], and spatial crypt visualizations were generated using ggplot2's geom_point() (Fig. 7b,f, Extended Data Fig. d,e). Cell-cell interaction analysis (Fig. 7h-3) was performed using

CellChat software [47] (conversion factor = 0.18; interaction range = 250; scale.distance = 4.5; contact range = 20).

Data explorer generation

All generated data were made available for interactive exploration using Vitessce [48]. For each individual sample, cell segmentation polygons were converted into a JSON format in which each cell is represented as an object containing a list of [x, y] coordinate pairs corresponding to its boundary vertices. The visualization interface included a “Spatial” viewer, which displays the sample in physical (x, y) space, allowing users to explore gene expression for any gene alongside cell-level annotations derived from downstream analyses. Additional panels included a “Quality Control” window showing violin plots for metrics such as transcripts per cell and unique genes per cell, a “Features” window listing available genes, and a “Cell Labels” window summarizing cell annotations. All panels were linked, enabling dynamic cross-filtering: selections made in one viewer were automatically reflected across the others. Files generated for the Vitessce viewers are hosted on Zenodo and the script used to generate these files was deposited on github (See **Data and Code Availability**).

Data and Code Availability

Raw sequences, images, and processed datasets from single-nuclei sequencing and spatial transcriptomics are available via Zenodo (link will be available upon acceptance), and code blocks used to analyze the data can be accessed in the GitHub repository (link will be available upon acceptance).

Acknowledgments

We thank the WorldQuant, GI Research Foundation, Bumrungrad International Hospital, the National Institutes of Health (R01MH117406), and the LLS (MCL 7001-18, LLS 9238-16, 7029-23). E.A., Y.Z., and A.F.R received funding from Angelini Ventures S.p.A. Rome, Italy. P.S.D. thanks NIDDK (1U01DK134321, 5R01DK135620), NIAID (1U19AI181102), and Digestive Health Foundation for the support.

We would like to acknowledge former SAHA members from NanoString Technologies, whose contribution was crucial for establishing and generating the early phase of the project, specifically Nathan Schurman, Joachim Schmid, Raymond Tecotzky, Sarah Church, and Charlie Glaser. Most importantly, we thank the patients and their family members who provided valuable samples for this research.

Author contributions

Conceptualization: J.P., C.E.M., R.E.S., S.L.H., A.A., R.D.G., E.H.

Patient sample coordination: E.H., B.R., S.P., F.S.,

Experiment and data generation: A.A., R.D.G., H.C., S.M., P.S.D., Y.L., L.P., K.Y., A.H., M.K., D.M., L.W., A.W.

Investigation and data visualization: J.P., E.O., N.B., F.S.D., L.Z., M.M., Y.Z., E.A., J.K., M.R.A., E.M., J.R., Jac.P., A.A.A., P.D.,
Supervision: C.E.M., R.E.S., S.L.H. A.F.R., J.T.P., L.M., O.E., G.C., M.L., J.B.
Writing: J.P., R.D.G., F.S.D., L.Z., Y.Z., A.F.R., E.A., A.A.A., E.O., N.B., J.T.P., C.E.M., S.B., S.R., P.D., S.M.L.
All authors discussed the results and contributed to the final manuscript.

Competing interests

C.E.M. serves on the Scientific Advisory Board of Cellanome Inc. Competing interests for G.C. is detailed here: https://arep.med.harvard.edu/gmc/tech.html. E.M., S.R., P.D., J.R., Y.L., L.P., S.B., K.Y., A.H., M.K., D.M., L.W., A.W., and J.B. are current/previous Bruker Spatial Biology employees.

SUPPLEMENTARY TABLES

Supplementary Table 1. SAHA Cohort Demographics and Clinical Metadata.
Summary of demographic and clinical characteristics of the SAHA cohort, including patient age, sex, tissue of origin, comorbidity (if applicable), and sample designation.

Supplementary Table 2. SAHA Experimental Run Metadata.
Detailed metadata for all SAHA spatial transcriptomics runs, including informations such as slide/sample identifiers, tissue types, assay panels, staining protocols, quality metrics/statistics, platform used (e.g., CosMx, Xenium), and batch/run identifiers.

Supplementary Table 3. Additional Information related to CRC Analysis.
Additional files regarding the CRC and COL comparative analysis including list of probe substitutes, differential gene expression lists, cell marker lists, full result list of Moran's I results.

FIGURES

Figure 1: Overview of SAHA Workflow and Data Scope.
a, Schematic overview of SAHA resource, summarizing sample collection and spatial profiles. The diagram illustrates the scale of (1) cohort, (2) organ types, (3) batches, (4) cells, and (5) biomolecules profiled across multiple platforms and modalities.
b, Heatmap showing the SAHA sample (healthy tissues) demographics across profiled organs, colored by age, sex, and ethnicity, with missing information labeled as unknown in gray.
c, Distribution of total cell numbers across healthy and diseased tissues stratified by technology and organ type; top right corner shows the summary of spatial technologies deployed (CosMx RNA and Protein, Xenium, GeoMx, RNAscope, H&E) with representative images from the same section in each category labeled with the same color.
d, Comparative overview of the published spatial atlases and SAHA by number of cells profiled, organ coverage, and assay modality (x axis). The dot size indicates the number of cells, and the colour indicates the maximum number of genes in the panel.

Figure 2: Key Structures, Cell Types, and Cellular Networks across SAHA Organs.
a, UMAP embeddings (n = 2,865,647 cells) colored by organ (top) or broad cell type (bottom).
b, Stacked violin plots showing canonical marker genes across major cell types, with color intensity reflecting median expression level.
c, Stacked bar chart summarizing the broad cell-type composition per section, illustrating the relative abundances of epithelial, immune, stromal, and neuronal cells.
d, Representative histological (H&E) sections, spatial RNA and protein images, and organ-specific UMAP embeddings from each tissue, demonstrating subcellular resolution and morphological context.

Figure 3: Spatial Neighborhoods and Cellular Niches of the Crypt.
a, Representative colon cross-section, showing spatially resolved cell types (colors represent cell types) across the mucosa, submucosa, and muscularis layers. Graphs to the right display the expression of key markers (e.g., *PIGR*, *MHC-I*, *ACTA2*) stratified by tissue depth.
b, Spatial enrichment scores of key biological pathways (keratinization, antigen processing, smooth muscle contraction) stratified by tissue depth.
c, Spatial mapping of proliferative and stress-response gene expressions (i.e., *CDKN1A*, *CCND1*, *TFEB*, and *SMARCB1*) within a magnified region at crypt boundaries.
d, Dot plot of enriched immune-epithelial crosstalk represented by ligand-receptor interactions from the crypt tip niche, sized by $-\log_2$ p-value.
e, Segmented overlays and heatmaps depicting cell type composition (e.g., strong T- and B-cell predominance near crypts, variable mesenchymal content deeper in the colon wall) across different tissue layers.
f, Cell type enrichment comparisons across all colon sections (left) and selected crypt regions, including colon cross-section (middle) and crypt tips (right).
g, Spatial projection of large lymphoid aggregates in SAHA APE, color-coded by cell type.
h, Force-directed graph showing adjacency networks among immune and stromal cells within lymphoid aggregates.

i, Spatial projections of cell types by both broad and detailed annotations, highlighting specialized immune subtypes (e.g., T follicular helper) and their heterogeneity.
j, Chord diagram and heatmaps of global and niche-specific ligand-receptor interactions, The left panels indicate overall interaction frequency among major cell types, while the right panels focus on specialized niches (e.g., lymphoid structures identified from APE).

Figure 4: Comparison of Spatial Neighborhoods and Cellular Niches across Organs.
a, Representative spatial mapping of lymphoid structures in SAHA lymph node (LN) samples, showing transcriptionally defined niches and cell type composition.
b, Bar plots comparing the proportion of B cells across “in GC (or lymphoid structure for appendix)” and “around GC” niches in LN and appendix (APE).
c, Spatial expression plots of canonical B cell markers (*MS4A1*, *IGHG1*) in LN and APE, illustrating organ-specific localization and expression intensity.
d, Cell-cell interaction matrices stratified by spatial niche showing overall interaction patterns around germinal centers.
e, Pathway enrichment analysis of genes shared between LN and APE that are both differentially expressed and spatially autocorrelated, showing enrichment for immune and follicular activation processes.
f, Top enriched pathways among APE-specific spatially variable DEGs, highlighting epithelial signaling and extracellular remodeling.
g, UMAP embedding of integrated gastrointestinal spatial datasets (APE, ILE, COL, STO), colored by tissue of origin and spatial neighborhood clusters.
h, Representative spatial projections showing neighborhood clustering across organs. Colors represent unbiased spatial clustering involving epithelial, immune, and stromal compartments.
i, Network graph illustrating relationships among organs, spatial neighborhood clusters, and broad cell types. Nodes represent variables (organ, spatial cluster, and cell type), colors of the edges represent edge weights (spatial connectivities), and the distance between nodes represents expression-level correlation.
j, Stacked bar chart of organ-specific distributions of spatial neighborhoods, where colors represent unbiased spatial clusters shown in **g-h**.
k, Relative frequencies of selected niche clusters, highlighting shared and organ-restricted spatial patterns; colors represent cell types.
l, Expression level (top) and spatial autocorrelation (bottom) comparison of selected genes across spatial neighborhoods, illustrating spatial heterogeneity and functional specialization within gastrointestinal tissue clusters.

Figure 5: Integration of Spatial Proteomics Data for Multi-omics Map
a, UMAP projection of normal SAHA spatial proteomics datasets from normal tissues following integration. Data are colored by tissue of origin (left), cell type labels using protein information (middle), and labels done with both RNA and protein information (right).
b, Heatmap of protein expression of RNA-derived cell type labels, showing canonical and cross-modality marker distributions.
c, Comparison of cell type assignments from RNA (top) and protein (bottom) datasets in representative fields of view.

d, Representative spatial images from SAHA PROS, APE, and STO tissues, comparing RNA-based (top) and protein-based (bottom) cell type assignments from the same fields of view.
e, Validation of ligand-receptor analysis using spatially resolved protein imaging, where protein expression of key immune markers (e.g., CCR7, HLA-DRA, CD4) overlaid on tissue sections (left) and ligand–receptor pair contributions based on spatially restricted analysis within selected regions (right) were shown.
f, Correlation plot of average RNA and protein expressions across overlapping markers..

Figure 6: Integration of Matched Histopathological imaging with Transcriptomics Data using Multimodal Foundation Models
a, Whole-slide H&E image of a representative SAHA slide (APE) showing tiled tissue regions used for feature extraction.
b, Schematic overview of the computational workflow: tissue regions are segmented, tesselated, and input to a multimodal foundation model that extracts quantitative morphological features for each region.
c, Low-dimensional embedding of image-derived morphological features using Isomap, showing tissue structure captured solely from histological patterns corresponding to morphologically-driven clusters.
d, Clustered heatmap of morphological feature embeddings across tissue locations, revealing spatial gradients and local heterogeneity.
e, Spatial reconstruction of tissue based on morphological clusters, demonstrating regional organization inferred from morphological features alone.
f, UMAP embedding of morphological tile clusters from the gastrointestinal tract (ileum, appendix, colon), with representative histological images from each cluster.
g, Organ-wise comparison of morphological clusters (top), annotated with similarity scores to histopathology terms (bottom), revealing conserved structures such as crypts, lymphoid follicles, and extracellular matrix regions.
h, Clustered heatmap showing enrichment of histopathological terms (rows) across morphology-derived clusters (columns), highlighting distinct text-derived phenotypes.
i, Composition of broad cell types (epithelial, connective, immune), segmented and classified in the histology images, within each morphology-derived cluster, revealing dominant biological compartments.
j, Pairwise distance matrix showing spatial proximity between clusters, with warmer colors indicating closer physical co-localization.
k, Canonical correlation analysis (CCA) comparing tile-level morphological cluster abundances with RNA-defined cell type abundances, showing correspondence between structure and cell states.
l, Example region from an H&E image (top) alongside matched CosMx cell-type annotation (bottom) illustrating alignment between morphological features and transcriptomics.

Figure 7: Spatial Heterogeneity in Cellular and Molecular Profiles Across Healthy Crypts from COL and CRC Samples.

a, UMAP projection of integrated healthy SAHA colon samples (SAHA COL, n=3) with colorectal cancer (CRC, n=1) following Harmony integration, colored by cell types (left) and disease status (right).
b, Representative spatial images from CRC tumor adjacent and SAHA COL tissues, colored by cell types.
c, Gene expression profiles of top and bottom crypt regions in SAHA COL and CRC tumor adjacent samples. Violin plots show normalized expression levels,-colored by disease status. Genes shared between SAHA COL and CRC samples (left) and differentially expressed genes in CRC tumor adjacent crypts (right) are shown.
d, K-means clustering of crypt FOVs based on spatially variable genes identified by Moran's I. Points are colored by sample status and shaded regions denote k-means clusters.
e, Comparison of spatially variable genes between CRC tumor adjacent and healthy crypts. Moran's I correlation plot from a representative CRC vs. SAHA COL FOV comparison (left) are shown, genes with Moran's I > 0.2 in either condition are highlighted in blue. Dashed red line indicates equal spatial autocorrelation. Violin plots of condition-specific spatial genes are shown (right).
f, Spatial expression of *IL22RA1* in healthy and CRC tumor adjacent crypts, representative of differentially enriched crypt genes in panel **e,** shown across normalized assay values; insets shown cell type annotations.
g, Intrapatient tumor heterogeneity in CRC sample, where H&E-stained section with annotated regions showing Type 1 (purple) and Type 2 (blue) tumor areas.
h, Lymphocyte-to-tumor cell ratio across FOVs, grouped by dominant tumor type calculated by the percentage of B cells and T cells divided by the tumor cell percentage in each FOV. Mixed denotes the FOV samples that have a close percentage of type 1 and type 2 tumor cells. Rest of the dots are colored based on the region of the tumor within the tissue.
i, Proportion of immune cell types in Type 1 vs. Type 2 tumor FOVs, colored by cell types that are manually curated.
j, Representative FOVs from each tumor type, colored by the cell type.
k, Spatial transcriptomics reveals unique perineural invasion (PNI) structure with great detail, demonstrated by H&E image of the corresponding PNI region (left) and spatial projection of cell types, where bright green highlights the glial cells that are surrounded by fibroblasts and tumor glands (right).
l, Dot plot of fibroblast markers highlighting the difference between close-contact fibroblasts to the nerve versus rest of the fibroblasts in the data.
m, Unique signaling interactions from close fibroblasts (ANGPTL pathway, left) and glial cells (LIFR pathway, right) toward immune and tumor compartments.

Figure 8: Application of the SAHA healthy ileum reference to spatially profile IBD tissues and therapeutic response.
a, Schematic overview of comparative analysis using SAHA ILE reference and ileal samples from IBD patients stratified by TNFα inhibitor response (Responder, Non-responder).
b, UMAP embeddings of CosMx RNA profiles colored by major cell types (left) and sample identities (right) across healthy ILE and IBD tissues.

c, Spatial mapping of cell types in representative IBD and healthy ileum sections, showing increased immune infiltration in IBD tissues.
d, Quantification of immune cell proximity to epithelial cells (within 300 µm), demonstrating significantly higher immune infiltration scores in IBD compared to healthy ileum (***$p < 0.001$).
e, Ligand-receptor interaction scores between immune and epithelial cells across IBD responders, non-responders, and healthy ileum, showing elevated spatial signaling in non-responders.
f, Violin plot of *TNFRSF1A* (TNF receptor 1) expression in mesenchymal-stromal cells across IBD responders, non-responders, and healthy ileum (**$p < 0.01$).
g, Spatial projection of TNF-TNFRSF1A ligand-receptor interactions in a representative IBD non-responder sample, highlighting immune–stromal interface activation.
h, Represented images of IBD and SAHA ILE samples (left) with UMAP embedding of unsupervised clustering of H&E-stained ileum sections, stratifying normal and IBD tissues based on morphological features (right).
i, Combined scores of histological features associated with IBD pathologies in responders and non-responders, including increased crypt branching, immune cell infiltration, and mucosal edema.

Figure 9: Impact of SAHA, SAHA Data Portal and Accessibility.
A, (to be updated) Comparison between traditional single-cell transcriptomic profiling (left) and spatial multi-omics profiling integrating morphological information (right), combining H&E staining, cell boundary segmentation, and multiplexed RNA and protein expression profiling (19k whole transcriptome probes + 67-plex protein).
b, Overview of cost and scalability considerations for spatial multi-omics at subcellular resolution.
c, SAHA data portal architecture, enabling integrated visualization and analysis of spatial multi-omics datasets. The portal supports interactive exploration of spatial transcriptomics and proteomics through UMAP and PCA projections, cell-type annotations, spatial imaging data, gene expression matrices, and downloadable formats including image files, flatfiles, AnnData, and Seurat objects for analysis in Python and R.

Fig. 1

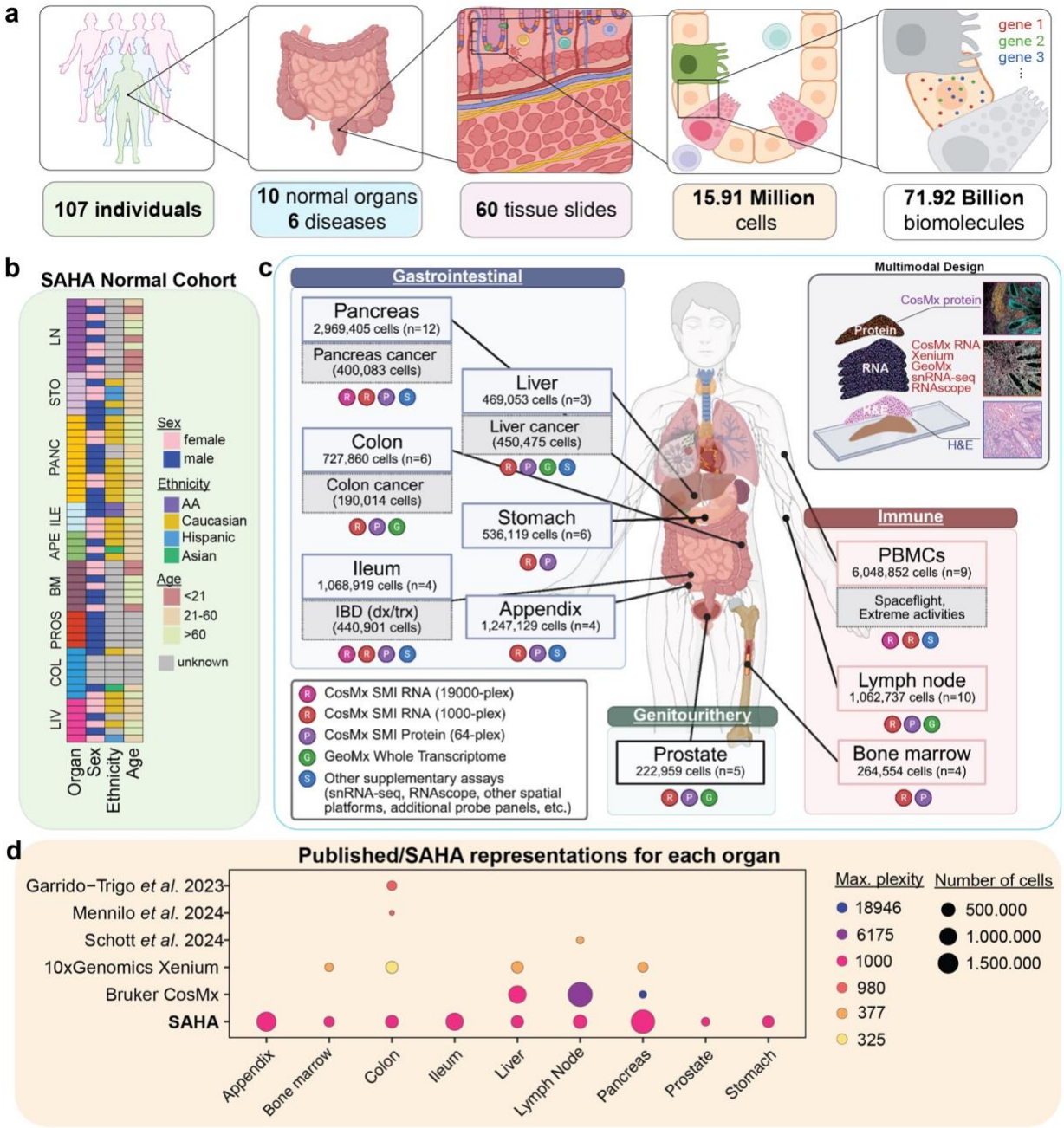
a
gene 1
gene 2
gene 3
107 individuals
10 normal organs
6 diseases
60 tissue slides
15.91 Million cells
71.92 Billion biomolecules
b
SAHA Normal Cohort
LN
STO
PANC
ILE
APE
BM
PROS
COL
LIV
Organ
Sex
Ethnicity
Age
Sex
female
male
Ethnicity
AA
Caucasian
Hispanic
Asian
Age
<21
21-60
>60
unknown
c
Gastrointestinal
Pancreas
2,969,405 cells (n=12)
Pancreas cancer
(400,083 cells)
Liver
469,053 cells (n=3)
Liver cancer
(450,475 cells)
Colon
727,860 cells (n=6)
Colon cancer
(190,014 cells)
Stomach
536,119 cells (n=6)
Ileum
1,068,919 cells (n=4)
IBD (dx/trx)
(440,901 cells)
Appendix
1,247,129 cells (n=4)
Genitourithery
Prostate
222,959 cells (n=5)
Immune
PBMCs
6,048,852 cells (n=9)
Spaceflight,
Extreme activities
Lymph node
1,062,737 cells (n=10)
Bone marrow
264,554 cells (n=4)
Multimodal Design
CosMx protein
Protein
RNA
CosMx RNA
Xenium
GeoMx
snRNA-seq
RNAscope
H&E
CosMx SMI RNA (19000-plex)
CosMx SMI RNA (1000-plex)
CosMx SMI Protein (64-plex)
GeoMx Whole Transcriptome
Other supplementary assays
(snRNA-seq, RNAscope, other spatial
platforms, additional probe panels, etc.)
d
Published/SAHA representations for each organ
Garrido−Trigo et al. 2023
Mennilo et al. 2024
Schott et al. 2024
10xGenomics Xenium
Bruker CosMx
SAHA
Appendix
Bone marrow
Colon
Ileum
Liver
Lymph Node
Pancreas
Prostate
Stomach
Max. plexity
18946
6175
1000
980
377
325
Number of cells
500.000
1.000.000
1.500.000

Fig. 2

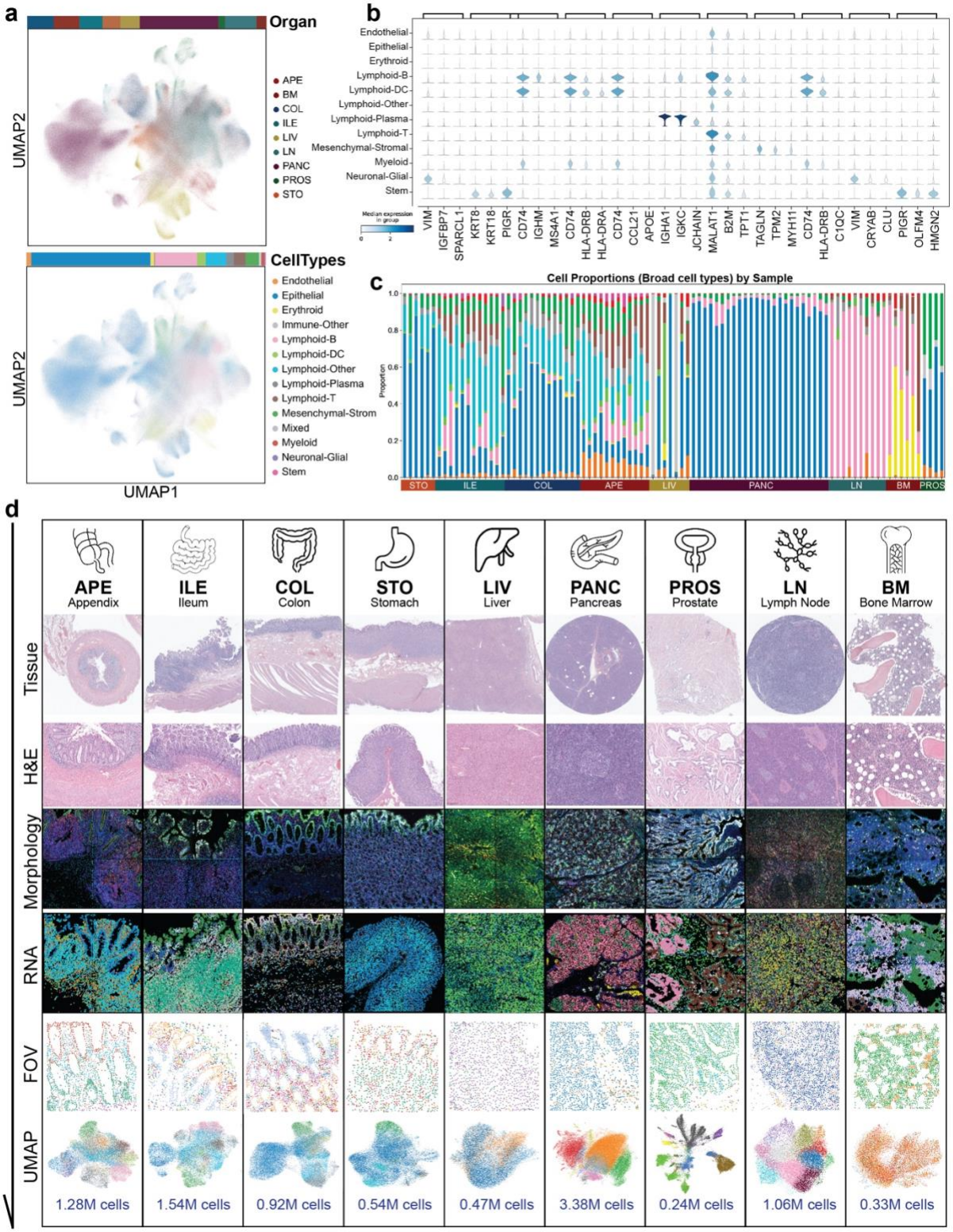
a
Organ
APE
BM
COL
ILE
LIV
LN
PANC
PROS
STO
UMAP2
CellTypes
Endothelial
Epithelial
Erythroid
Immune-Other
Lymphoid-B
Lymphoid-DC
Lymphoid-Other
Lymphoid-Plasma
Lymphoid-T
Mesenchymal-Strom
Mixed
Myeloid
Neuronal-Glial
Stem
UMAP1
b
Endothelial
Epithelial
Erythroid
Lymphoid-B
Lymphoid-DC
Lymphoid-Other
Lymphoid-Plasma
Lymphoid-T
Mesenchymal-Stromal
Myeloid
Neuronal-Glial
Stem
VIM
IGFBP7
SPARCL1
KRT8
KRT18
PIGR
CD74
IGHM
MS4A1
CD74
HLA-DRB
HLA-DRA
CD74
CCL21
APOE
IGHA1
IGKC
JCHAIN
MALAT1
B2M
TPT1
TAGLN
TPM2
MYH11
CD74
HLA-DRB
C1QC
VIM
CRYAB
CLU
PIGR
OLFM4
HMGN2
c
Cell Proportions (Broad cell types) by Sample
Proportion
STO
ILE
COL
APE
LIV
PANC
LN
BM
PROS
d
APE Appendix
ILE Ileum
COL Colon
STO Stomach
LIV Liver
PANC Pancreas
PROS Prostate
LN Lymph Node
BM Bone Marrow
Tissue
H&E
Morphology
RNA
FOV
UMAP
1.28M cells
1.54M cells
0.92M cells
0.54M cells
0.47M cells
3.38M cells
0.24M cells
1.06M cells
0.33M cells

Fig. 3

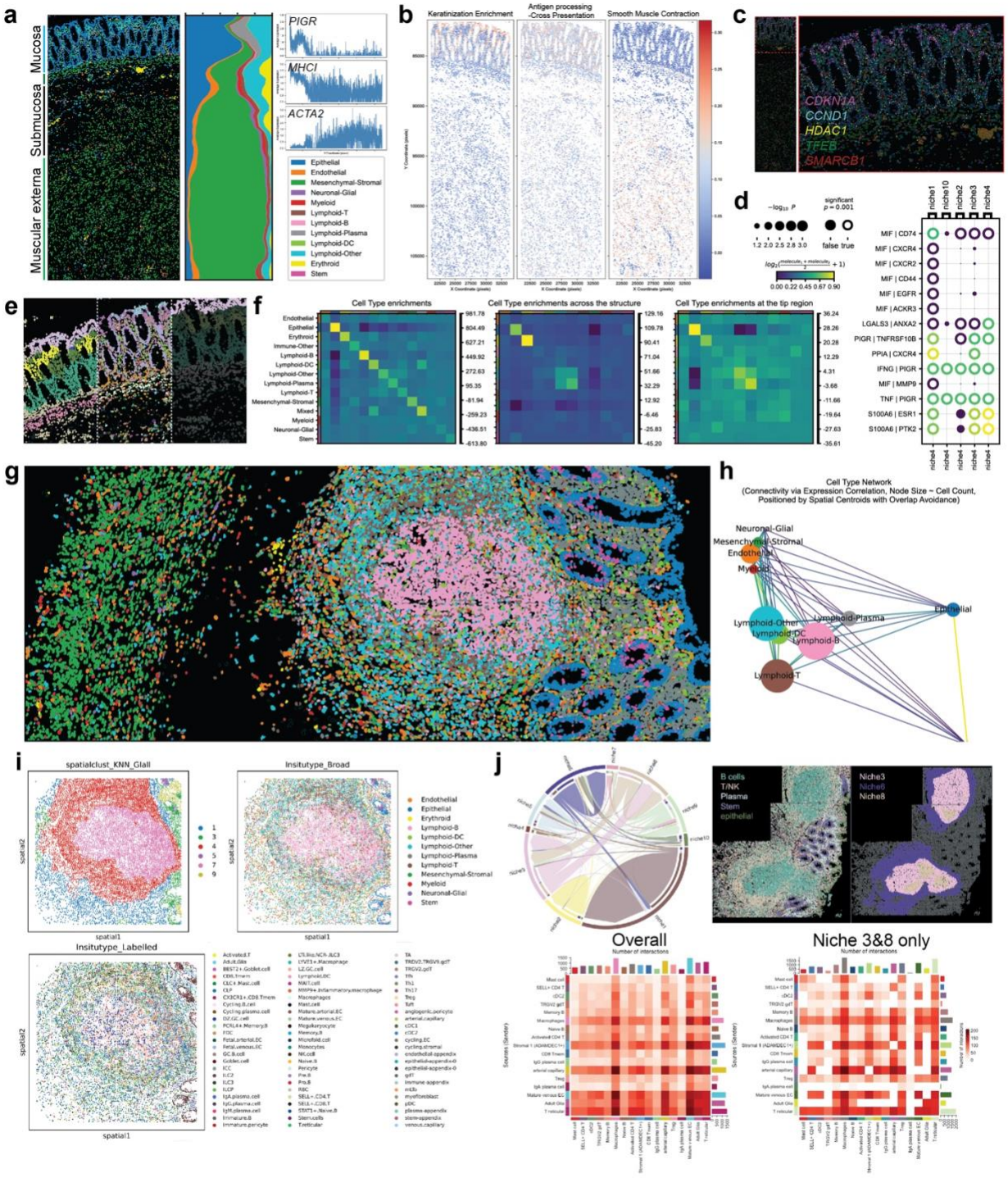
a
Mucosa
Submucosa
Muscular externa
PIGR
MHCI
ACTA2
Epithelial
Endothelial
Mesenchymal-Stromal
Neuronal-Glial
Myeloid
Lymphoid-T
Lymphoid-B
Lymphoid-Plasma
Lymphoid-DC
Lymphoid-Other
Erythroid
Stem
b
Keratinization Enrichment
Antigen processing -Cross Presentation
Smooth Muscle Contraction
c
CDKN1A
CCND1
HDAC1
TFEB
SMARCB1
d
niche1
niche10
niche2
niche3
niche4
MIF | CD74
MIF | CXCR4
MIF | CXCR2
MIF | CD44
MIF | EGFR
MIF | ACKR3
LGALS3 | ANXA2
PIGR | TNFRSF10B
PPIA | CXCR4
IFNG | PIGR
MIF | MMP9
TNF | PIGR
S100A6 | ESR1
S100A6 | PTK2
e
f
Cell Type enrichments
Cell Type enrichments across the structure
Cell Type enrichments at the tip region
Endothelial
Epithelial
Erythroid
Immune-Other
Lymphoid-B
Lymphoid-DC
Lymphoid-Other
Lymphoid-Plasma
Lymphoid-T
Mesenchymal-Stromal
Mixed
Myeloid
Neuronal-Glial
Stem
g
h
Cell Type Network
(Connectivity via Expression Correlation, Node Size ~ Cell Count, Positioned by Spatial Centroids with Overlap Avoidance)
Neuronal-Glial
Mesenchymal-Stromal
Endothelial
Myeloid
Epithelial
Lymphoid-Plasma
Lymphoid-Other
Lymphoid-DC
Lymphoid-B
Lymphoid-T
i
spatialclust_KNN_Glall
Insitutype_Broad
Insitutype_Labelled
spatial1
spatial2
j
B cells
T/NK
Plasma
Stem
epithelial
Niche3
Niche6
Niche8
Overall
Niche 3&8 only
Number of interactions

1256 **Fig. 4**

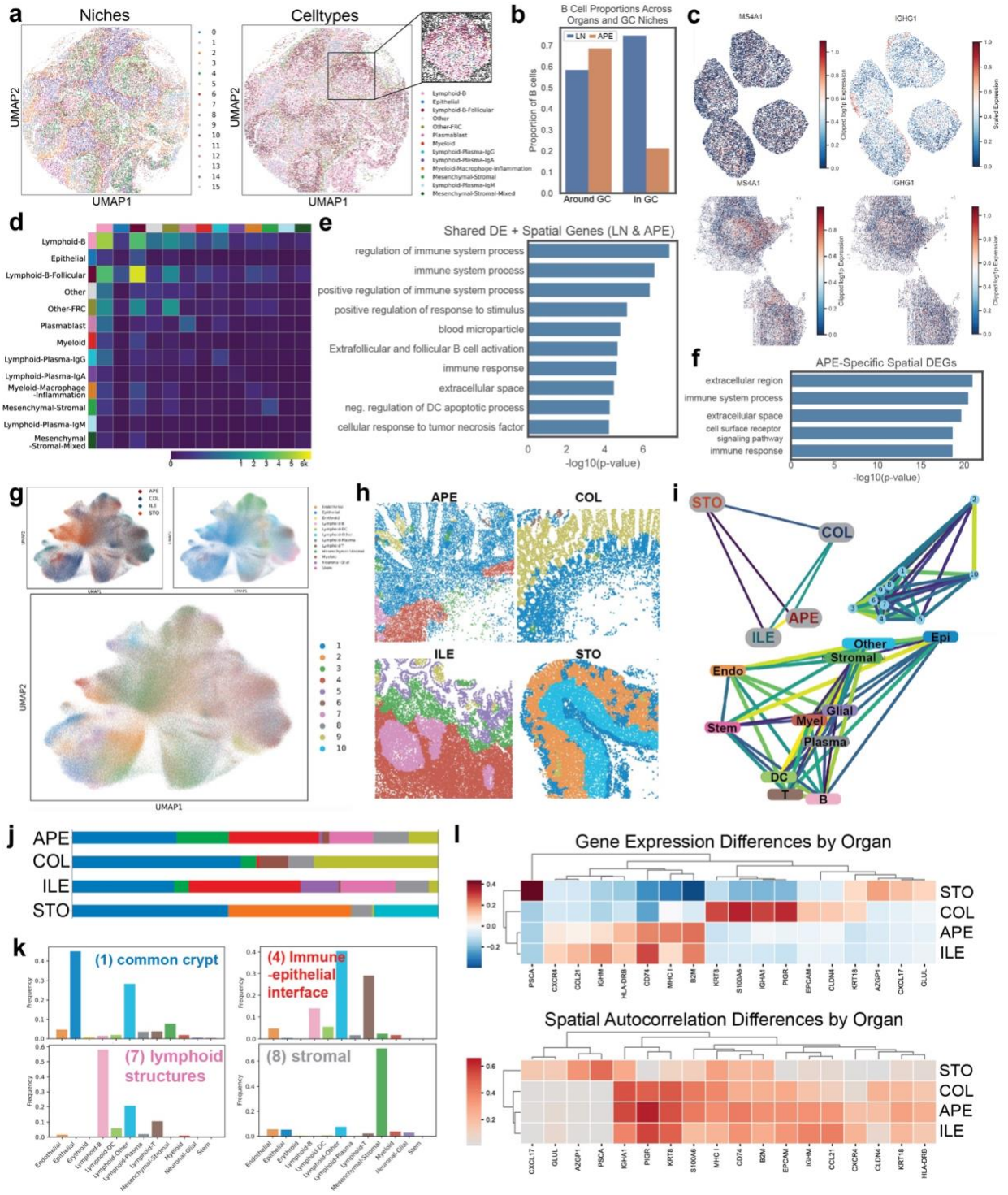

1257

Fig. 5

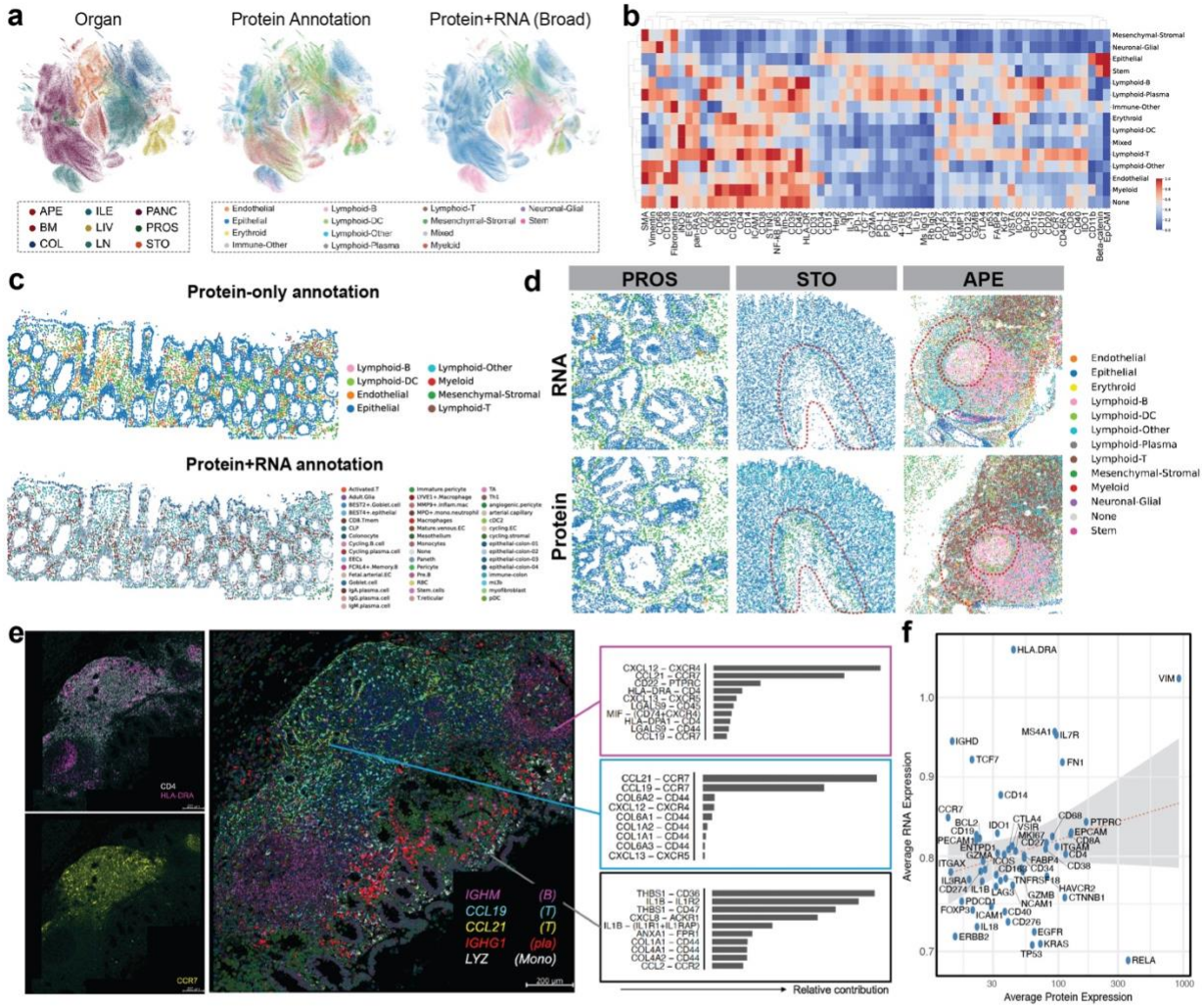

a
Organ
Protein Annotation
Protein+RNA (Broad)
APE
ILE
PANC
BM
LIV
PROS
COL
LN
STO
b
c
Protein-only annotation
Protein+RNA annotation
d
PROS
STO
APE
RNA
Protein
e
IGHM (B)
CCL19 (T)
CCL21 (T)
IGHG1 (pla)
LYZ (Mono)
Relative contribution
f
Average RNA Expression
Average Protein Expression

Fig. 6

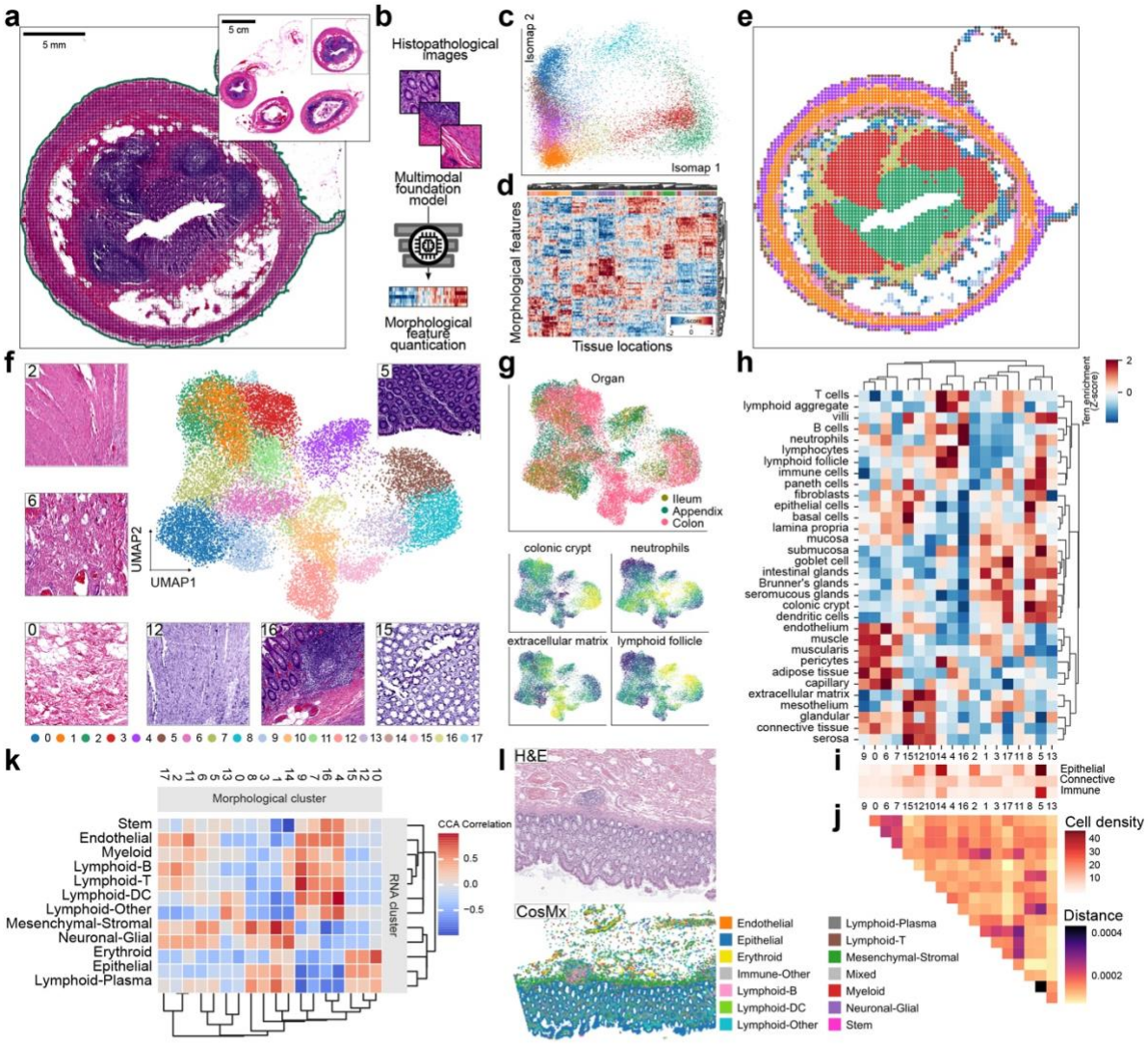
a
5 mm
5 cm
b
Histopathological images
Multimodal foundation model
Morphological feature quantication
c
Isomap 2
Isomap 1
d
Morphological features
Tissue locations
e
f
UMAP2
UMAP1
g
Organ
Ileum
Appendix
Colon
colonic crypt
neutrophils
extracellular matrix
lymphoid follicle
h
Term enrichment (Z-score)
T cells
lymphoid aggregate
villi
B cells
neutrophils
lymphocytes
lymphoid follicle
immune cells
paneth cells
fibroblasts
epithelial cells
basal cells
lamina propria
mucosa
submucosa
goblet cell
intestinal glands
Brunner's glands
seromucous glands
colonic crypt
dendritic cells
endothelium
muscle
muscularis
pericytes
adipose tissue
capillary
extracellular matrix
mesothelium
glandular
connective tissue
serosa
i
Epithelial
Connective
Immune
j
Cell density
Distance
k
Morphological cluster
RNA cluster
CCA Correlation
Stem
Endothelial
Myeloid
Lymphoid-B
Lymphoid-T
Lymphoid-DC
Lymphoid-Other
Mesenchymal-Stromal
Neuronal-Glial
Erythroid
Epithelial
Lymphoid-Plasma
l
H&E
CosMx
Endothelial
Epithelial
Erythroid
Immune-Other
Lymphoid-B
Lymphoid-DC
Lymphoid-Other
Lymphoid-Plasma
Lymphoid-T
Mesenchymal-Stromal
Mixed
Myeloid
Neuronal-Glial
Stem

Fig. 7

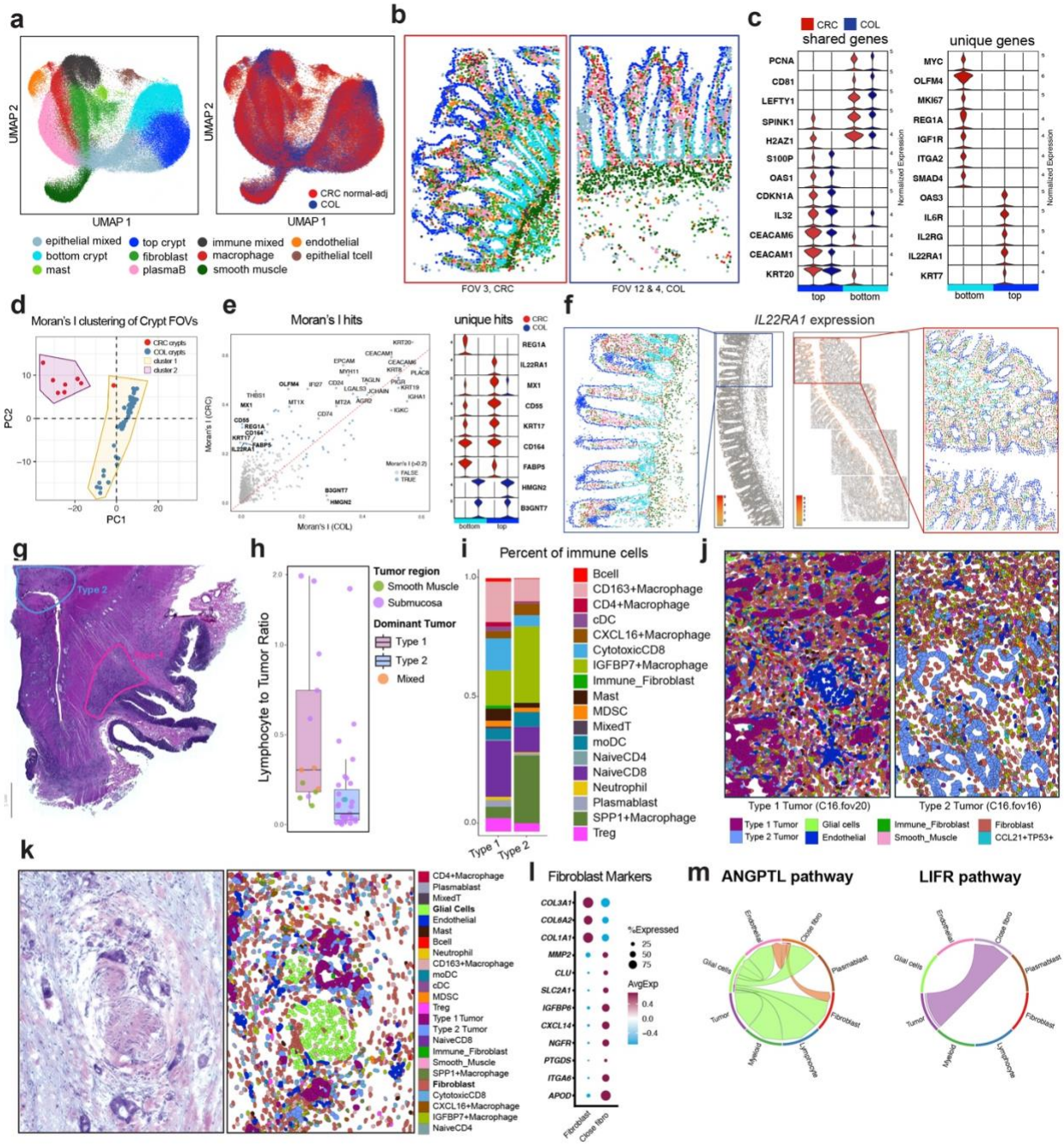
a
UMAP 2
UMAP 1
CRC normal-adj
COL
epithelial mixed
bottom crypt
mast
top crypt
fibroblast
plasmaB
immune mixed
macrophage
smooth muscle
endothelial
epithelial tcell
b
FOV 3, CRC
FOV 12 & 4, COL
c
CRC
COL
shared genes
unique genes
PCNA
CD81
LEFTY1
SPINK1
H2AZ1
S100P
OAS1
CDKN1A
IL32
CEACAM6
CEACAM1
KRT20
MYC
OLFM4
MKI67
REG1A
IGF1R
ITGA2
SMAD4
OAS3
IL6R
IL2RG
IL22RA1
KRT7
Normalized Expression
top
bottom
d
Moran's I clustering of Crypt FOVs
CRC crypts
COL crypts
cluster 1
cluster 2
PC1
PC2
e
Moran's I hits
Moran's I (CRC)
Moran's I (COL)
unique hits
REG1A
IL22RA1
MX1
CD55
KRT17
CD164
FABP5
HMGN2
B3GNT7
f
IL22RA1 expression
g
Type 2
Type 1
h
Lymphocyte to Tumor Ratio
Tumor region
Smooth Muscle
Submucosa
Dominant Tumor
Type 1
Type 2
Mixed
i
Percent of immune cells
Type 1
Type 2
Bcell
CD163+Macrophage
CD4+Macrophage
cDC
CXCL16+Macrophage
CytotoxicCD8
IGFBP7+Macrophage
Immune_Fibroblast
Mast
MDSC
MixedT
moDC
NaiveCD4
NaiveCD8
Neutrophil
Plasmablast
SPP1+Macrophage
Treg
j
Type 1 Tumor (C16.fov20)
Type 2 Tumor (C16.fov16)
Type 1 Tumor
Type 2 Tumor
Glial cells
Endothelial
Immune_Fibroblast
Smooth_Muscle
Fibroblast
CCL21+TP53+
k
CD4+Macrophage
Plasmablast
MixedT
Glial Cells
Endothelial
Mast
Bcell
Neutrophil
CD163+Macrophage
moDC
cDC
MDSC
Treg
Type 1 Tumor
Type 2 Tumor
NaiveCD8
Immune_Fibroblast
Smooth_Muscle
SPP1+Macrophage
Fibroblast
CytotoxicCD8
CXCL16+Macrophage
IGFBP7+Macrophage
NaiveCD4
l
Fibroblast Markers
COL3A1
COL6A2
COL1A1
MMP2
CLU
SLC2A1
IGFBP6
CXCL14
NGFR
PTGDS
ITGA6
APOD
Fibroblast
Close fibro
%Expressed
25
50
75
AvgExp
0.4
0.0
−0.4
m
ANGPTL pathway
LIFR pathway
Endothelial
Close fibro
Plasmablast
Fibroblast
Lymphocyte
Myeloid
Tumor
Glial cells

1264 **Fig. 8**

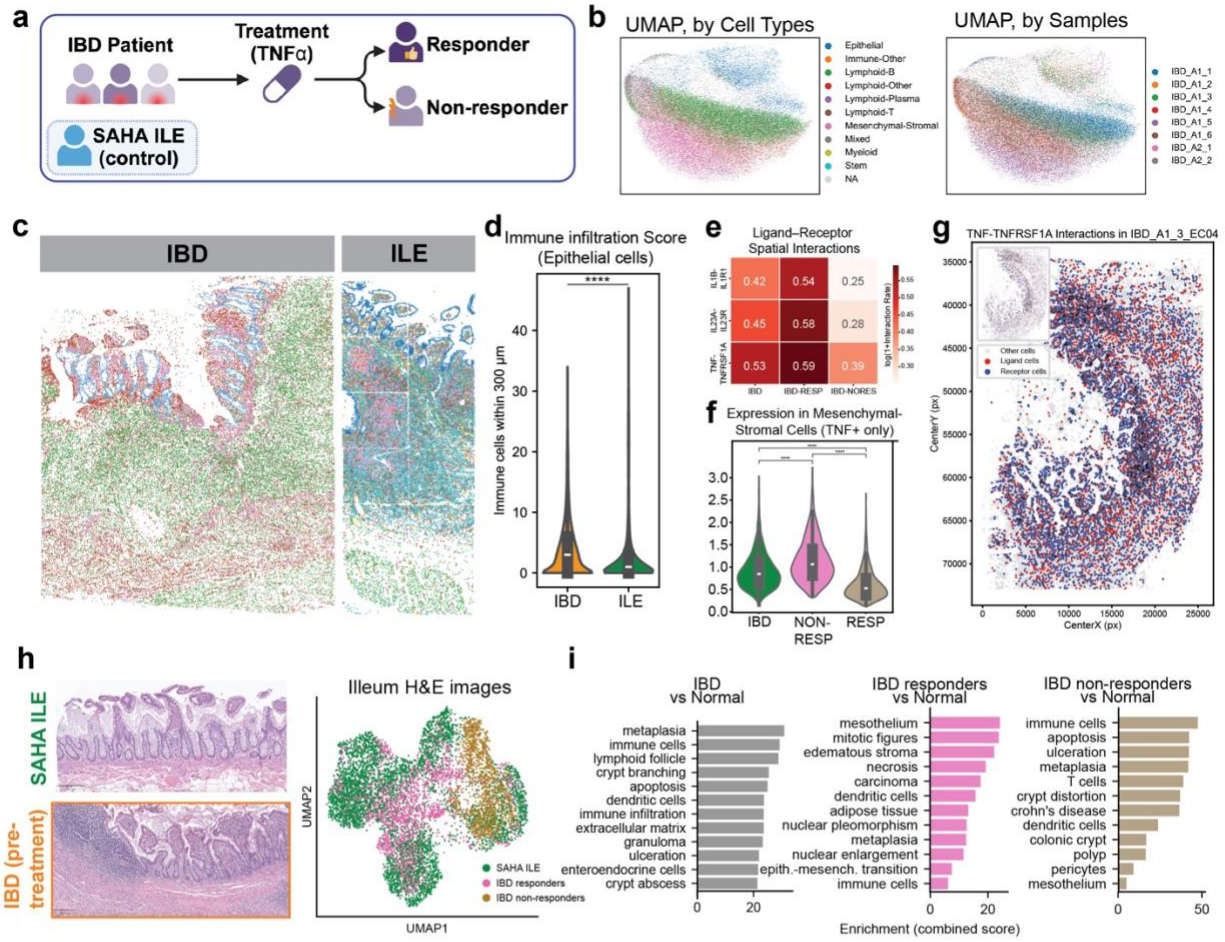

1265

Fig. 9

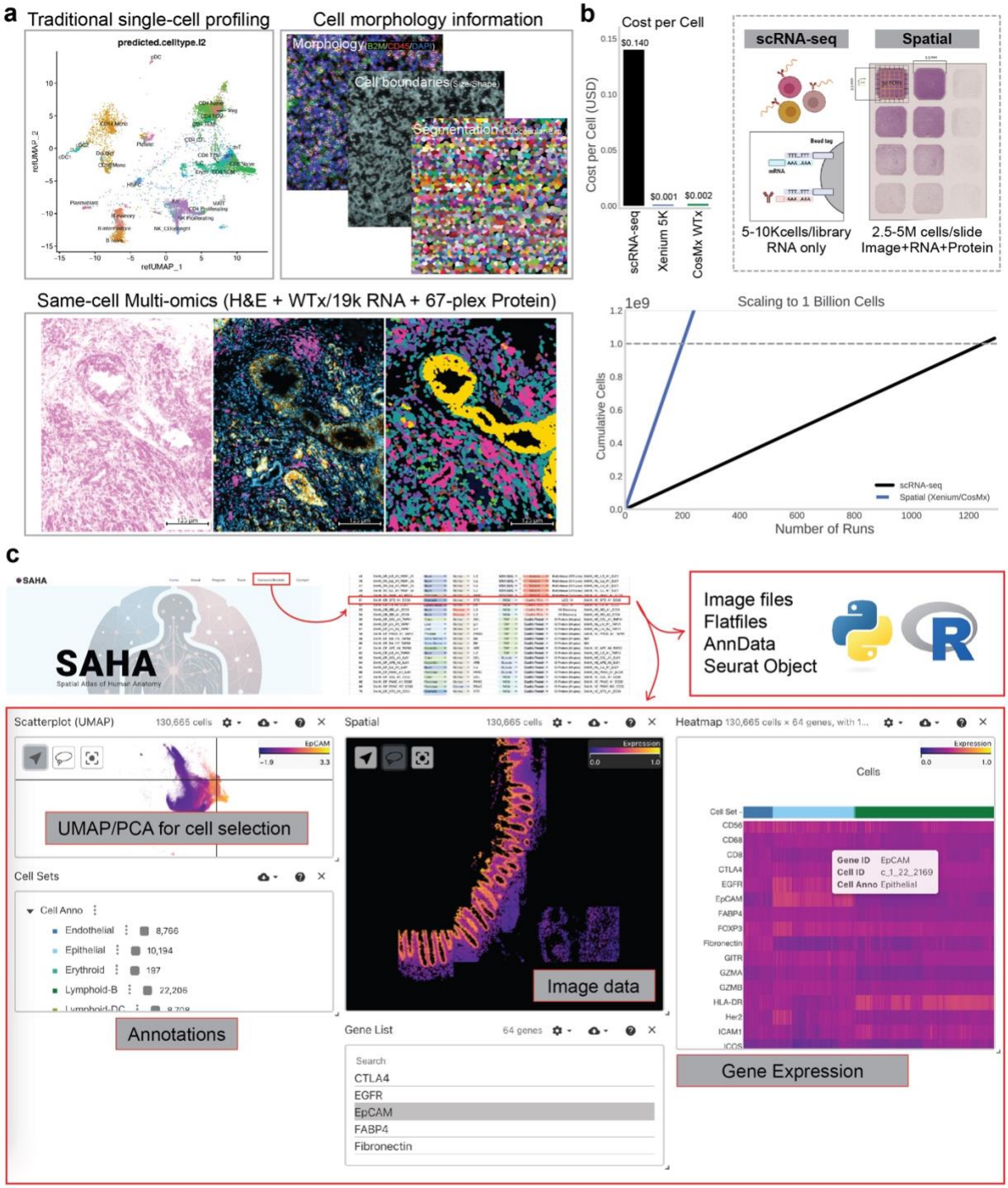
a
Traditional single-cell profiling
Cell morphology information
predicted.celltype.l2
Morphology
Cell boundaries
Segmentation
Same-cell Multi-omics (H&E + WTx/19k RNA + 67-plex Protein)
b
Cost per Cell
Cost per Cell (USD)
$0.140
$0.001
$0.002
scRNA-seq
Xenium 5K
CosMx WTx
scRNA-seq
Spatial
5-10Kcells/library
RNA only
2.5-5M cells/slide
Image+RNA+Protein
Scaling to 1 Billion Cells
Cumulative Cells
Number of Runs
scRNA-seq
Spatial (Xenium/CosMx)
c
SAHA
Spatial Atlas of Human Anatomy
Image files
Flatfiles
AnnData
Seurat Object
Scatterplot (UMAP)
130,665 cells
UMAP/PCA for cell selection
Cell Sets
Cell Anno
Endothelial 8,766
Epithelial 10,194
Erythroid 197
Lymphoid-B 22,206
Annotations
Spatial
Image data
Gene List
64 genes
Search
CTLA4
EGFR
EpCAM
FABP4
Fibronectin
Heatmap 130,665 cells × 64 genes, with 1...
Cells
Gene ID EpCAM
Cell ID c_1_22_2169
Cell Anno Epithelial
Gene Expression

EXTENDED DATA FIGURES AND TABLES

Extended Data Fig. 1: SAHA project workflow and data generation pipeline.
Overview of tissue collection, sample preparation, multimodal spatial profiling (CosMx, Xenium, GeoMx, RNAscope, snPATHO-seq), data integration, and open-access portal deployment.

Extended Data Fig. 2: Detailed Cell Types Identified from SAHA.
a, UMAP projections colored by detailed cell-type annotations derived from canonical marker gene expression.
b, Stacked bar charts showing detailed cell-type composition across sections and the relative abundance of epithelial, immune, stromal, and neuronal subtypes.
c, Organ-specific distribution of broad cell types (epithelial, immune, stromal, neuronal, etc.).

Extended Data Fig. 3: Overall Quality Assessment of SAHA Data.
a, Representative RNAscope segmentation and quantification results.
b, Comparison of RNAscope mean transcript counts of control probe PPIB (left) versus CosMx RNA mean counts for matched samples (right).
c, Correlation analyses (Spearman's ρ, top) and Bland-Altman plots (bottom) assessing agreement between RNAscope and CosMx measurements. CosMx RNA mean counts (left) and CosMx RNA feature counts (right) across samples were compared, and each dot represents a sample. Grey dashed lines represent the linear regression fit with shaded areas indicating the 95% confidence intervals. For Bland-Altman analysis, the x-axis represents the mean of the two measurements, and the y-axis shows the difference (CosMx – RNAscope), where each sample is labeled with its sample ID number, and the grey dashed line indicates the mean difference (bias), and red dashed lines indicate the 95% limits of agreement (mean ± 1.96 × SD).
d, Quality control metrics compared across gastrointestinal organ cohorts, demonstrating consistent assay performance.

Extended Data Fig. 4: Spatial mapping of lymphoid structures and cellular neighborhoods in the appendix.
a, Spatial expression patterns of highly variable genes (*IGHA1, IGKC, CD74, CCL21*) highlighting lymphoid structures in SAHA APE as an example.
b, Spatial projections of cellular neighborhoods and detailed cell types across representative fields of view (FOVs) in SAHA APE, colored by cell type and spatial neighborhoods (left); representative spatial projection of lymphoid structure showing distributions of spatial neighborhoods (middle) and broad and granular cell types (right) in a single FOV.

Extended Data Fig. 5: Cellular diversity and spatial neighborhood organization in SAHA lymph nodes.
a, UMAP embeddings of SAHA LN B cell niches (left) and transcriptionally defined cell types (right), including Lymphoid-B, Follicular B, Plasma subsets, and stromal components.
b, Heatmap showing normalized expression (z-score) of B cell and plasma cell marker genes across annotated LN cell types, highlighting class-switching and activation gradients.

c, Spatial projections of LN section showing annotated GC and peri-GC regions used for niche comparison. Cells not used in GC analysis are shaded in gray.
d, Cell-cell interaction matrices stratified by cell types revealing distinct interaction patterns in germinal center, relative to **Fig. 4d**.
e, Expression projections of selected differentially expressed genes in GC vs. peri-GC cells.
f, Volcano plot comparing GC vs. peri-GC B cells in LN, showing significantly upregulated (red) and downregulated (blue) genes.
g, Spatial projections of colon (top) and LN (bottom) samples colored by broad cell type annotations.
h, UpSet plot showing intersecting gene sets between differentially expressed genes (DEGs) and spatially variable genes across LN and colon GC niches. Shared and unique signatures highlight conserved and tissue-specific B cell programs.

Extended Data Fig. 6: Spatial network architecture and immune-epithelial interactions across gastrointestinal tissues.
a, Spatial network statistics (average clustering coefficient, closeness centrality, degree centrality) across SAHA APE, ILE, COL, and STO tissues.
b, Co-occurrence analysis of epithelial cells with other cell types within crypt-associated regions.
c, Top ligand–receptor interactions between immune and epithelial cells within lymphoid structures.
d, Comparison of various spatial neighborhood clustering methods across APE, ILE, and COL crypt structures.
e, Significant immune-epithelial ligand-receptor interactions across gastrointestinal organs.

Extended Data Fig. 7: Comparison of RNA and protein expression across tissues and validation of annotation consistency.
a, Hierarchical cell type classification scheme used for protein-based phenotyping with SciMap.
b, Cell type proportions across major organs based on protein-based annotations.
c, Comparison of cell type assignments from RNA (top) and protein (bottom) data from **Fig. 5c**.
d, Label concordance between MaxFuse-integrated annotations and SciMap gating-based annotations confirming consistent cell type classification across platforms.
e, Scatter plots of average RNA versus protein expression across matched genes for each organ, showing tissue-specific correlation patterns. Each dot represents a gene with paired RNA and protein measurements; red line indicates linear regression, and shaded area denotes 95% confidence interval.
f, Zoomed-in views for representative genes with different RNA–protein concordance profiles.

Extended Data Fig. 8: Integrated spatial annotation and cell-type resolution in CRC and SAHA COL samples.
a, Violin plots showing the raw distribution of detected features and counts across CRC and SAHA COL samples.
b, Dot plot of cell-type specific marker genes used for annotation in the integrated dataset of CRC and SAHA COL samples. Dot size corresponds to the percentage of cells within a cluster expressing the gene, and the color represents the scaled gene expression level. Clusters

labeled “mixed” and “Epithelial_tcell” include expression patterns that may represent multiple cell types likely due to segmentation artifacts.

c, Bar plots showing the overall percentage and the number of cells across CRC and SAHA COL.

d, Representative FOVs from CRC and SAHA COL, colored by cell types from panel **c**.

e, Expression maps showing examples of CRC-enriched spatially variable genes identified in **Fig. 7e**. Expression of *REG1A* and *MX1* is shown across CRC and SAHA COL FOVs.

f, UMAP projection of CRC sample (n=1), colored by the cell types.

g, Dot plot of marker genes used to identify CRC clusters. Dot size corresponds to the percentage of cells expressing the gene within each cluster and color shows the scaled expression value.

h, Perineural invasion (PNI) FOV clustered independently to resolve fibroblast subtypes. Close-contact fibroblasts adjacent to the nerve are distinguished (purple) from other fibroblast populations (red).

Extended Data Fig. 9: Cell-type level comparisons between SAHA healthy ileum and IBD tissues.

a, Spearman correlation matrix of cell-type average expression profiles between 1000-plex (lower-plex) and 6000-plex (higher-plex) CosMx RNA datasets, clustered by broad and detailed cell types. Higher correlation values indicate consistent cell-type transcriptional programs across datasets.

b, UMAP embedding of detailed cell-type annotations derived from CosMx RNA profiling, colored by cell type.

c, Heatmap showing relative cell-type composition across individual samples from healthy ileum (ILE) and IBD tissues, stratified by sample ID.

d, Stacked bar plots summarizing cell-type composition aggregated by clinical condition (healthy ileum, IBD responder, IBD non-responder), highlighting changes in epithelial, immune, and stromal populations between healthy and disease states.

1385 **Extended Data Fig. 1**

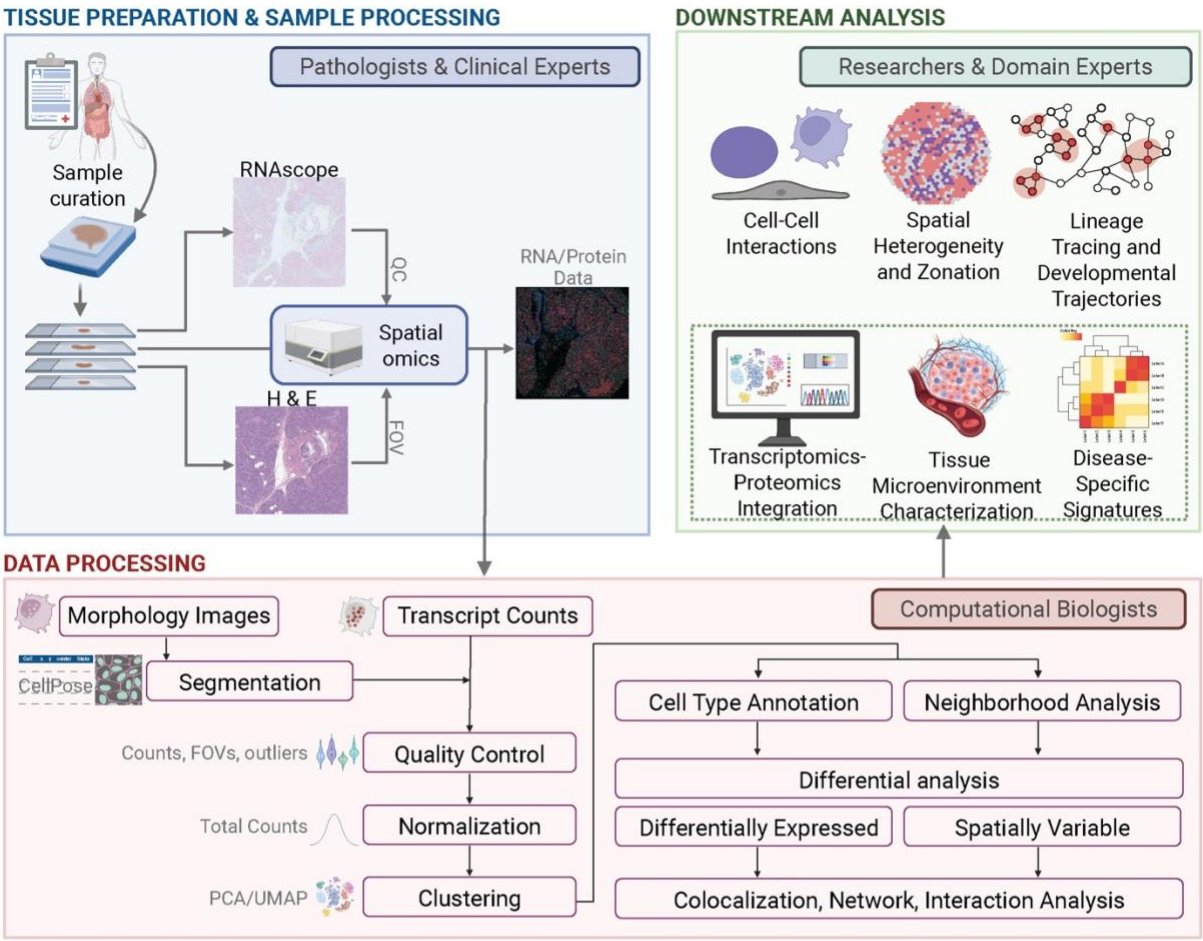

1386

Extended Data Fig. 2

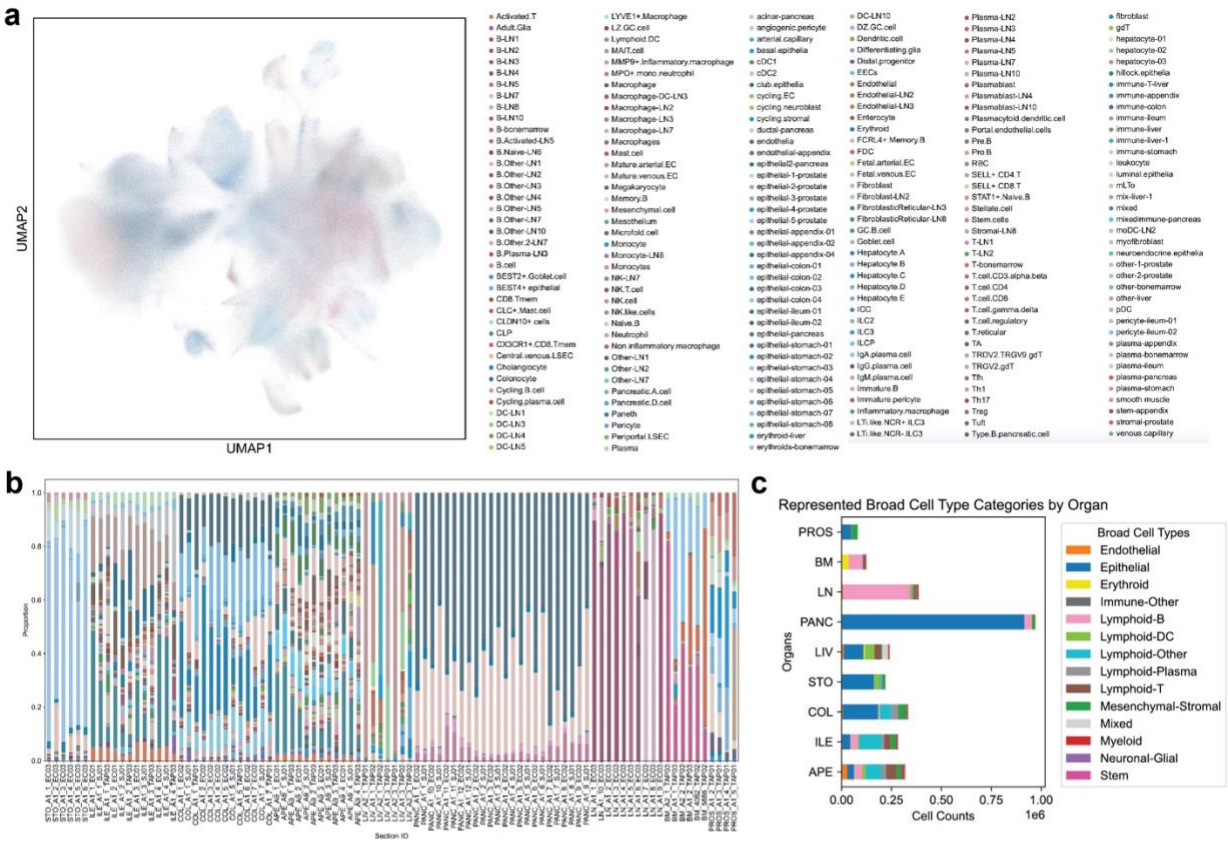

Extended Data Fig. 3

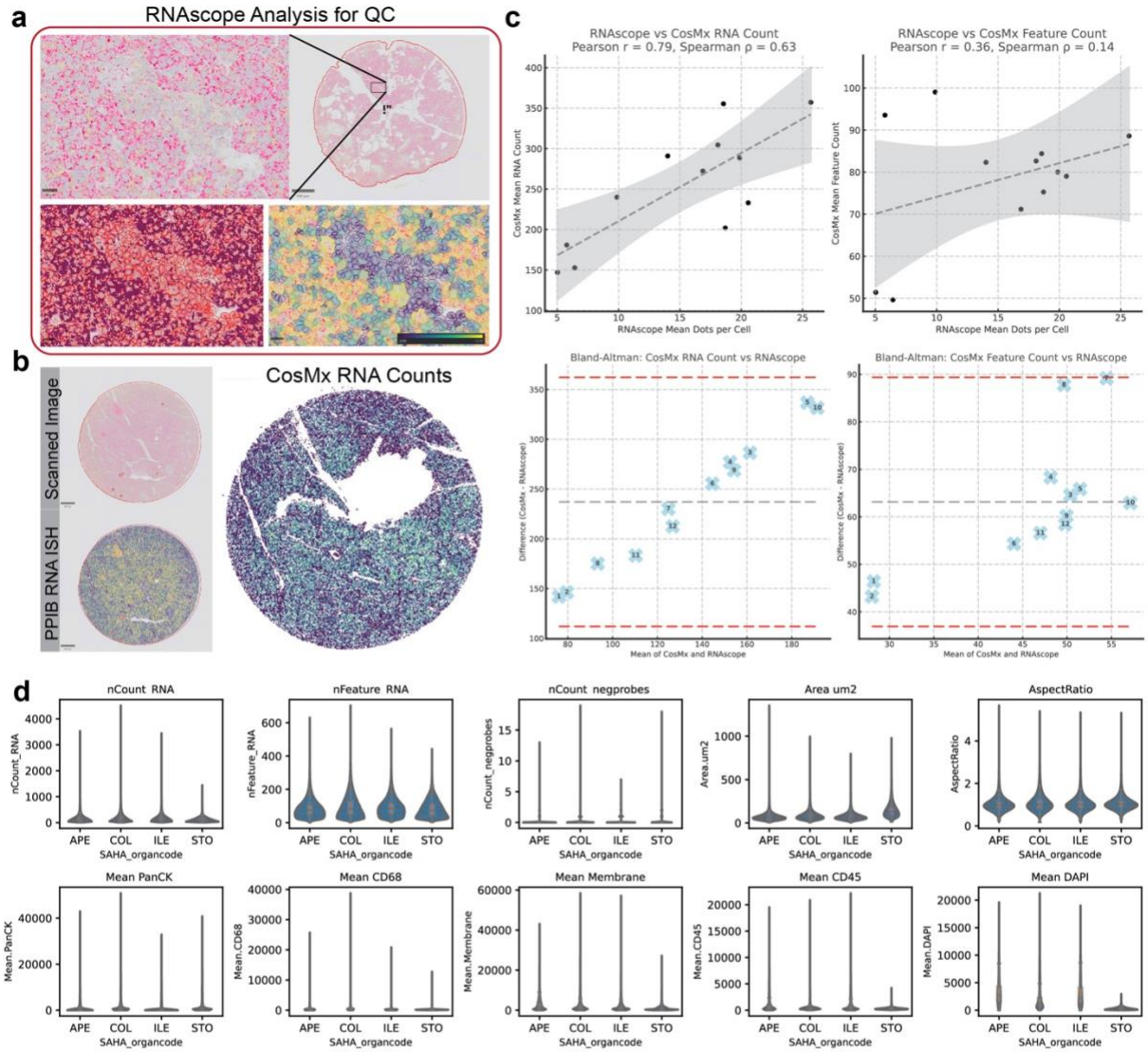

1391 **Extended Data Fig. 4**

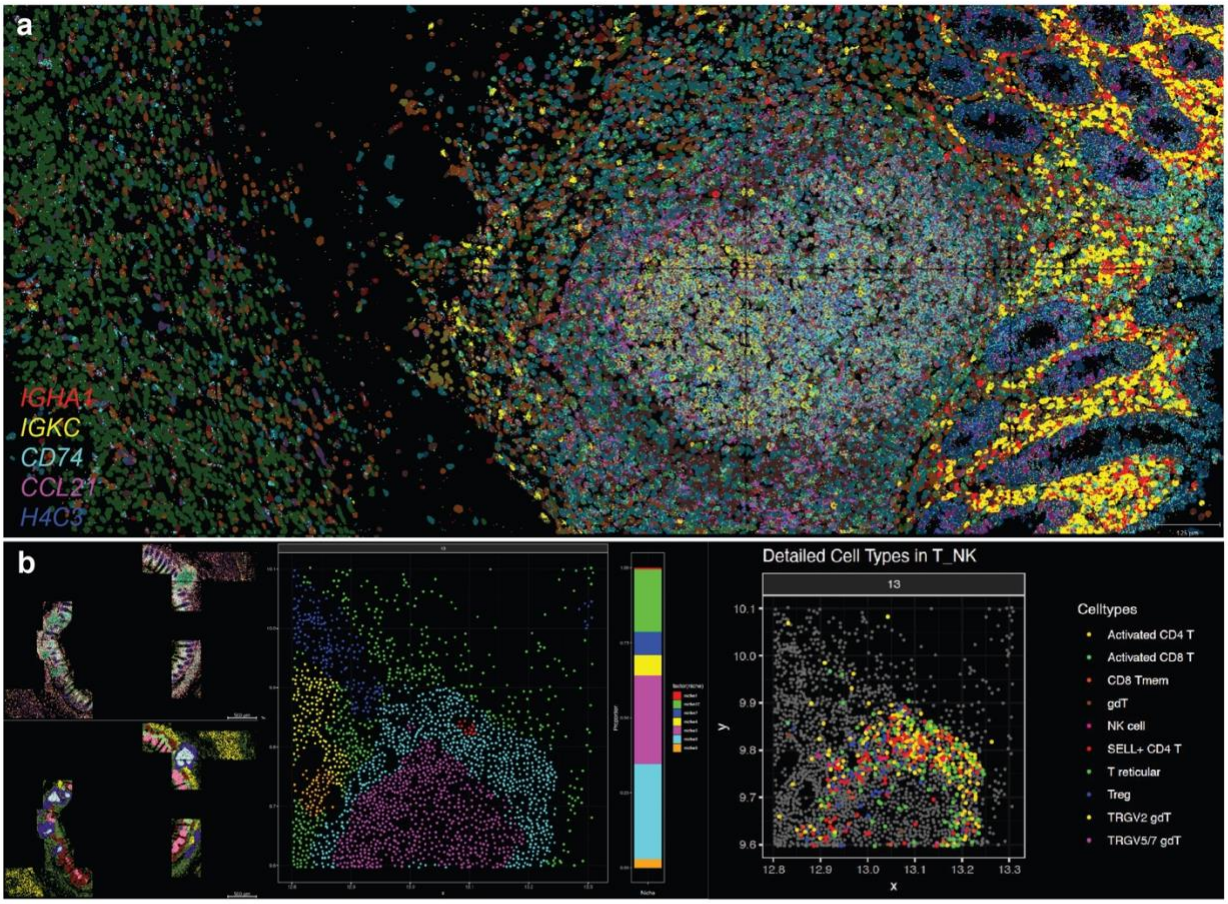

1392

Extended Data Fig. 5

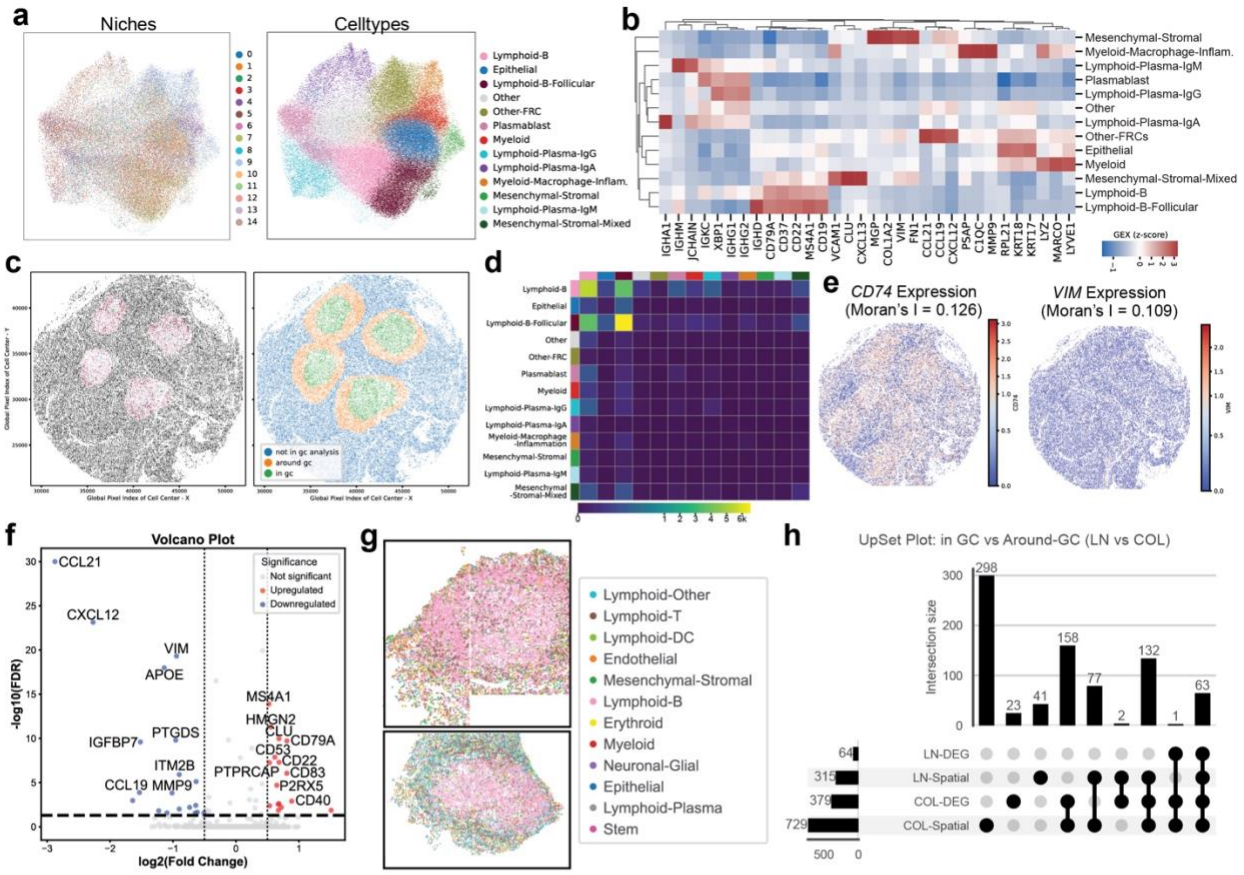

Extended Data Fig. 6

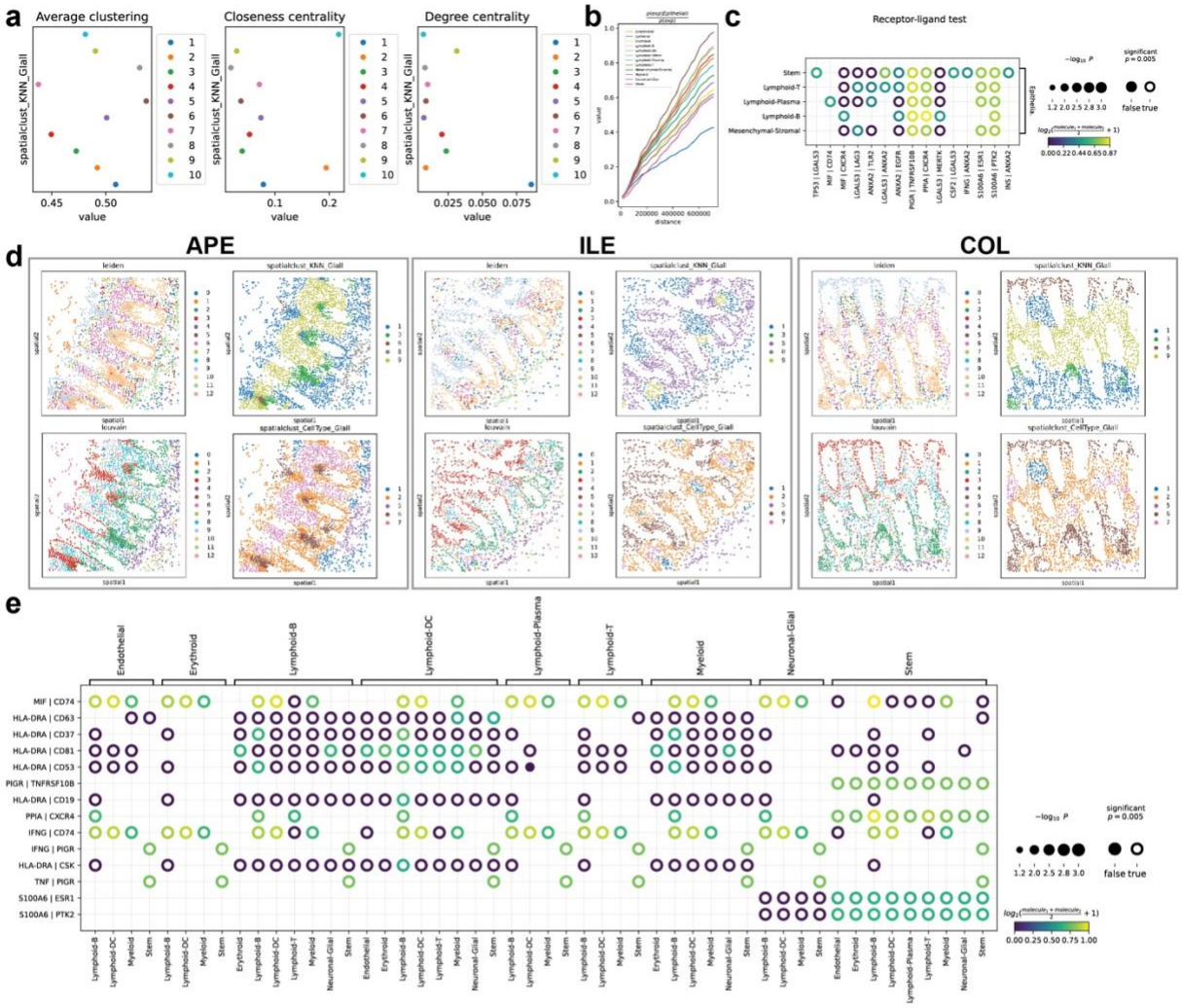

Extended Data Fig. 7

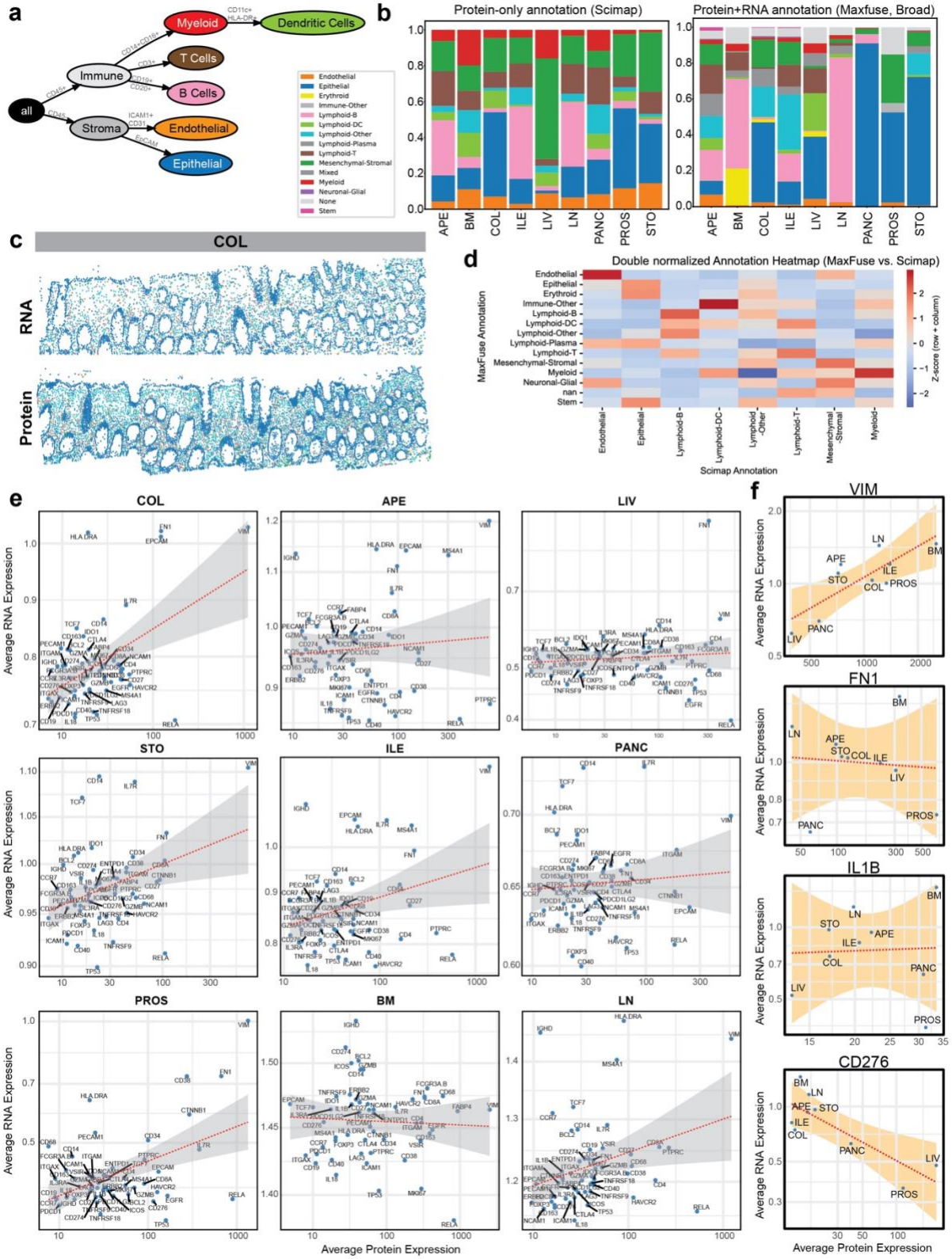

Extended Data Fig. 8

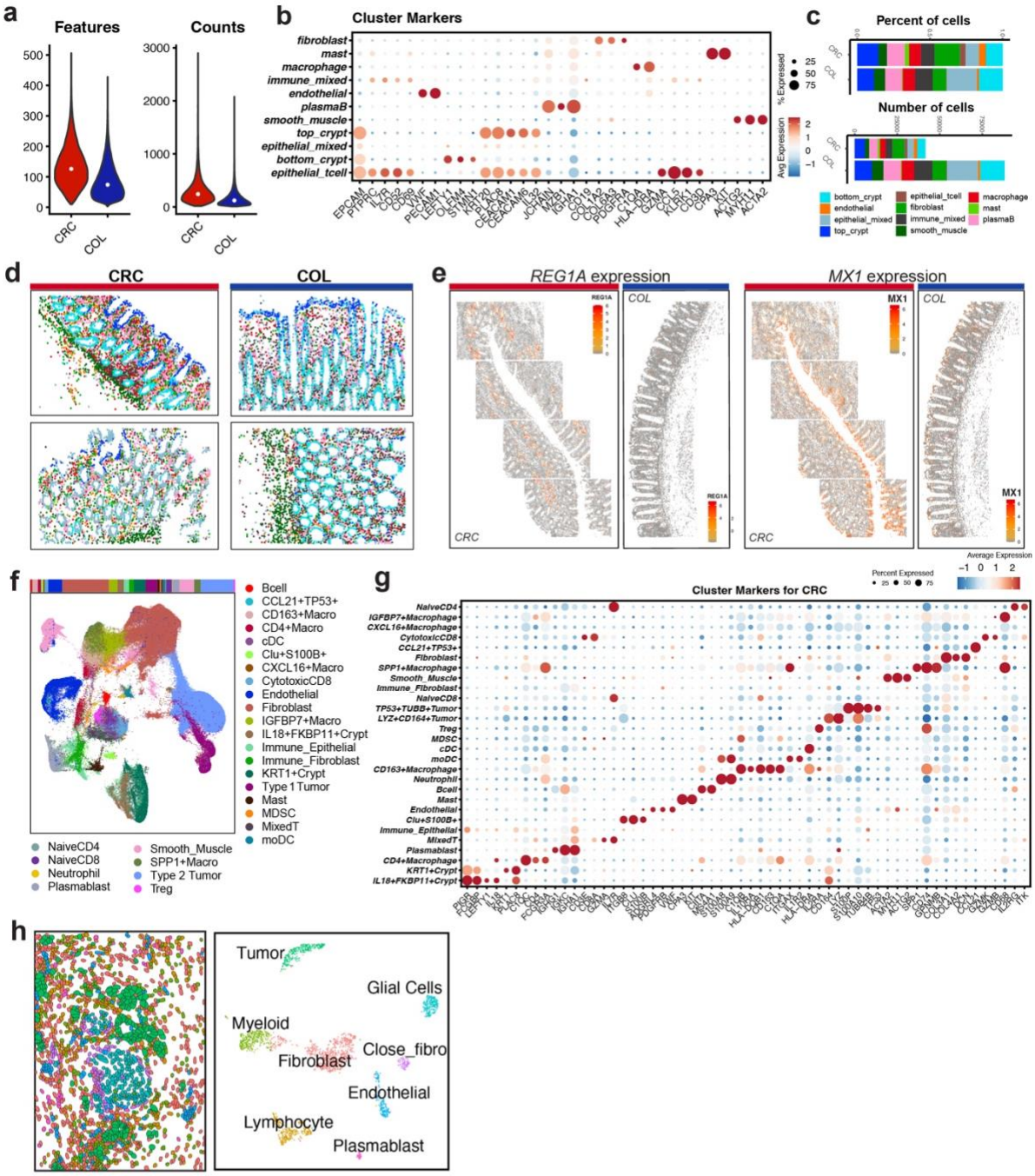

1401 **Extended Data Fig. 9**

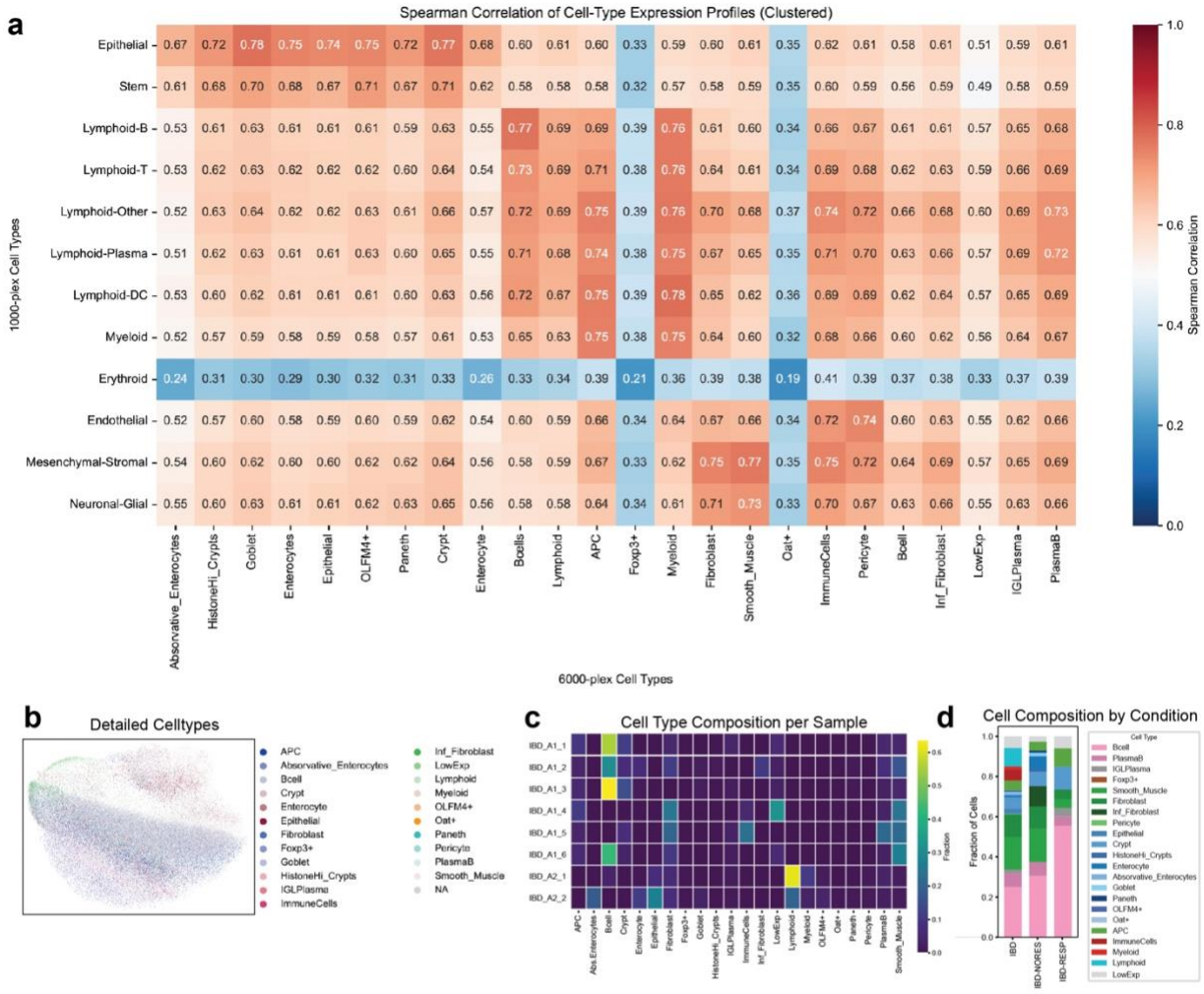

1402

1403 **REFERENCES**

1404 1. Palla, G., Fischer, D. S., Regev, A. & Theis, F. J. Spatial components of molecular tissue
1405 biology. *Nat. Biotechnol.* **40**, 308–318 (2022).
1406 2. Park, J. *et al.* Spatial omics technologies at multimodal and single cell/subcellular level.
1407 *Genome Biol.* **23**, 256 (2022).
1408 3. Rood, J. E. *et al.* The Human Cell Atlas from a cell census to a unified foundation model.
1409 *Nature* **637**, 1065–1071 (2025).
1410 4. Rozenblatt-Rosen, O. *et al.* The Human Tumor Atlas Network: Charting Tumor Transitions
1411 across Space and Time at Single-Cell Resolution. *Cell* **181**, 236–249 (2020).
1412 5. Velten, B. & Stegle, O. Principles and challenges of modeling temporal and spatial omics
1413 data. *Nat. Methods* **20**, 1462–1474 (2023).
1414 6. Cook, D. P. *et al.* A Comparative Analysis of Imaging-Based Spatial Transcriptomics
1415 Platforms. *BioRxiv* (2023) doi:10.1101/2023.12.13.571385.
1416 7. Wilkinson, M. D. *et al.* The FAIR Guiding Principles for scientific data management and
1417 stewardship. *Sci. Data* **3**, 160018 (2016).
1418 8. Liu, X. *et al.* Spatial multi-omics: deciphering technological landscape of integration of multi-
1419 omics and its applications. *J. Hematol. Oncol.* **17**, 72 (2024).
1420 9. Yu, Y., Mai, Y., Zheng, Y. & Shi, L. Assessing and mitigating batch effects in large-scale
1421 omics studies. *Genome Biol.* **25**, 254 (2024).
1422 10. Chen, S. *et al.* Integration of spatial and single-cell data across modalities with weak
1423 linkage. *BioRxiv* (2023) doi:10.1101/2023.01.12.523851.
1424 11. Novoselsky, R. *et al.* Intracellular polarization of RNAs and proteins in the human small
1425 intestinal epithelium. *PLoS Biol.* **22**, e3002942 (2024).
1426 12. Liu, S. *et al.* The role of CD276 in cancers. *Front. Oncol.* **11**, 654684 (2021).
1427 13. Lu, M. Y. *et al.* A visual-language foundation model for computational pathology. *Nat. Med.*
1428 **30**, 863–874 (2024).

1429 14. Liu, Y. & Chen, Y.-G. Intestinal epithelial plasticity and regeneration via cell
1430 dedifferentiation. *Cell Regen (Lond)* **9**, 14 (2020).
1431 15. Bala, P. *et al.* Aberrant cell state plasticity mediated by developmental reprogramming
1432 precedes colorectal cancer initiation. *Sci. Adv.* **9**, eadf0927 (2023).
1433 16. Koltsova, E. K. & Grivennikov, S. I. IL-22 gets to the stem of colorectal cancer. *Immunity*
1434 **40**, 639–641 (2014).
1435 17. Waldner, M. J., Foersch, S. & Neurath, M. F. Interleukin-6--a key regulator of colorectal
1436 cancer development. *Int. J. Biol. Sci.* **8**, 1248–1253 (2012).
1437 18. Liu, X., Li, X., Wei, H., Liu, Y. & Li, N. Mast cells in colorectal cancer tumour progression,
1438 angiogenesis, and lymphangiogenesis. *Front. Immunol.* **14**, 1209056 (2023).
1439 19. Xue, M. *et al.* Schwann cells regulate tumor cells and cancer-associated fibroblasts in the
1440 pancreatic ductal adenocarcinoma microenvironment. *Nat. Commun.* **14**, 4600 (2023).
1441 20. Zhang, B. *et al.* Single-cell RNA sequencing reveals intratumoral heterogeneity and
1442 potential mechanisms of malignant progression in prostate cancer with perineural invasion.
1443 *Front. Genet.* **13**, 1073232 (2022).
1444 21. Zhang, Z. *et al.* Integrating clinical and genetic analysis of perineural invasion in head and
1445 neck squamous cell carcinoma. *Front. Oncol.* **9**, 434 (2019).
1446 22. Chen, H. *et al.* ANGPTL1 attenuates colorectal cancer metastasis by up-regulating
1447 microRNA-138. *J. Exp. Clin. Cancer Res.* **36**, 78 (2017).
1448 23. Jiang, K. *et al.* Exosomal ANGPTL1 attenuates colorectal cancer liver metastasis by
1449 regulating Kupffer cell secretion pattern and impeding MMP9 induced vascular leakiness. *J.*
1450 *Exp. Clin. Cancer Res.* **40**, 21 (2021).
1451 24. Chang, T.-Y., Lan, K.-C., Chiu, C.-Y., Sheu, M.-L. & Liu, S.-H. ANGPTL1 attenuates cancer
1452 migration, invasion, and stemness through regulating FOXO3a-mediated SOX2 expression
1453 in colorectal cancer. *Clin. Sci.* **136**, 657–673 (2022).
1454 25. Tang, W. *et al.* LIF/LIFR oncogenic signaling is a novel therapeutic target in endometrial

1455 cancer. *Cell Death Discov.* **7**, 216 (2021).
1456 26. Oliver, A. J. *et al.* Single-cell integration reveals metaplasia in inflammatory gut diseases.
1457 *Nature* **635**, 699–707 (2024).
1458 27. Zhang, J. *et al.* Tahoe-100M: A Giga-Scale Single-Cell Perturbation Atlas for Context-
1459 Dependent Gene Function and Cellular Modeling. *BioRxiv* (2025)
1460 doi:10.1101/2025.02.20.639398.
1461 28. He, S. *et al.* High-Plex Multiomic Analysis in FFPE Tissue at Single-Cellular and Subcellular
1462 Resolution by Spatial Molecular Imaging. *BioRxiv* (2021) doi:10.1101/2021.11.03.467020.
1463 29. Wang, T. *et al.* snPATHO-seq, a versatile FFPE single-nucleus RNA sequencing method to
1464 unlock pathology archives. *Commun. Biol.* **7**, 1340 (2024).
1465 30. Butler, A., Hoffman, P., Smibert, P., Papalexi, E. & Satija, R. Integrating single-cell
1466 transcriptomic data across different conditions, technologies, and species. *Nat. Biotechnol.*
1467 **36**, 411–420 (2018).
1468 31. Satija, R., Farrell, J. A., Gennert, D., Schier, A. F. & Regev, A. Spatial reconstruction of
1469 single-cell gene expression data. *Nat. Biotechnol.* **33**, 495–502 (2015).
1470 32. Hao, Y. *et al.* Dictionary learning for integrative, multimodal and scalable single-cell
1471 analysis. *Nat. Biotechnol.* **42**, 293–304 (2024).
1472 33. Stuart, T. *et al.* Comprehensive Integration of Single-Cell Data. *Cell* **177**, 1888-1902.e21
1473 (2019).
1474 34. Hao, Y. *et al.* Integrated analysis of multimodal single-cell data. *Cell* **184**, 3573-3587.
1475 (2021).
1476 35. Germain, P.-L., Lun, A., Garcia Meixide, C., Macnair, W. & Robinson, M. D. Doublet
1477 identification in single-cell sequencing data using scDblFinder. *F1000Res.* **10**, 979 (2021).
1478 36. Bankhead, P. *et al.* QuPath: Open source software for digital pathology image analysis. *Sci.*
1479 *Rep.* **7**, 16878 (2017).
1480 37. Danaher, P. *et al.* Insitutype: likelihood-based cell typing for single cell spatial

1481 transcriptomics. *BioRxiv* (2022) doi:10.1101/2022.10.19.512902.

1482 38. Korsunsky, I. *et al.* Fast, sensitive and accurate integration of single-cell data with
1483 Harmony. *Nat. Methods* **16**, 1289–1296 (2019).

1484 39. Tian, T., Zhang, J., Lin, X., Wei, Z. & Hakonarson, H. Dependency-aware deep generative
1485 models for multitasking analysis of spatial omics data. *Nat. Methods* **21**, 1501–1513 (2024).

1486 40. Zheng, Y., Abila, E., Chrenková, E., Winkler, J. & Rendeiro, A. F. LazySlide: accessible and
1487 interoperable whole slide image analysis. *BioRxiv* (2025) doi:10.1101/2025.05.28.656548.

1488 41. McInnes, L., Healy, J. & Melville, J. UMAP: Uniform Manifold Approximation and Projection
1489 for Dimension Reduction. *arXiv* (2018) doi:10.48550/arxiv.1802.03426.

1490 42. Traag, V. A., Waltman, L. & van Eck, N. J. From Louvain to Leiden: guaranteeing well-
1491 connected communities. *Sci. Rep.* **9**, 5233 (2019).

1492 43. Wolf, F. A., Angerer, P. & Theis, F. J. SCANPY: large-scale single-cell gene expression
1493 data analysis. *Genome Biol.* **19**, 15 (2018).

1494 44. Hörst, F. *et al.* CellViT: Vision Transformers for precise cell segmentation and classification.
1495 *Med. Image Anal.* **94**, 103143 (2024).

1496 45. Moses, L. *et al.* Voyager: exploratory single-cell genomics data analysis with geospatial
1497 statistics. *BioRxiv* (2023) doi:10.1101/2023.07.20.549945.

1498 46. Bunis, D. G., Andrews, J., Fragiadakis, G. K., Burt, T. D. & Sirota, M. dittoSeq: universal
1499 user-friendly single-cell and bulk RNA sequencing visualization toolkit. *Bioinformatics* **36**,
1500 5535–5536 (2021).

1501 47. Jin, S. *et al.* Inference and analysis of cell-cell communication using CellChat. *Nat.*
1502 *Commun.* **12**, 1088 (2021).

1503 48. Keller, M. S. *et al.* Vitessce: integrative visualization of multimodal and spatially resolved
1504 single-cell data. *Nat. Methods* **22**, 63–67 (2025).